

1 **THE EFFECT OF PRESSURE ON ACOUSTIC (1-20 KHZ) VELOCITY AND**
2 **ATTENUATION DURING THE MELTING OF ICE-BEARING SAND**

3
4 Hanif S. Sutyoso^{1,2,*}, Sourav K. Sahoo², Ismael H. Falcon-Suarez², Laurence J.

5 North², Timothy A. Minshull¹, Angus I. Best²

6
7 ¹School of Ocean and Earth Science, University of Southampton, Southampton, UK.

8 ²National Oceanography Centre Southampton, Southampton, UK.

9 *Corresponding author: Hanif S. Sutyoso, hanifsans@noc.ac.uk,

10 <https://orcid.org/0000-0002-3111-2414>

11
12 **ABSTRACT**

13 Acoustic velocity and attenuation in ice-bearing sediments are strongly influenced by
14 ice and water saturations and can vary with frequency, but the mechanisms linking acoustic
15 response to ice content and morphology remain poorly understood. We measured velocity and
16 attenuation in ice-bearing sand using an acoustic pulse tube, which allowed multifrequency
17 analysis, under effective pressures of 2.5, 5.0, and 7.5 megapascals. Our experiments simulated
18 thawing permafrost conditions at depths of up to 450 meters. As the ice melted, acoustic
19 velocity decreased and attenuation increased, with the most pronounced changes observed at
20 lower pressures. These changes also varied with frequency, especially at higher frequencies.
21 Comparisons with three-phase Biot models suggest that velocity is mainly affected by ice
22 saturation, while attenuation is also influenced by ice morphology (i.e., whether it is pore-filling
23 or cementing) and by the permeability of the sediment frame. These results demonstrate that
24 low-frequency acoustic measurements under controlled conditions can provide insights into the
25 effects of ice saturation, distribution, and morphology on acoustic behavior in ice-bearing
26 sediments that are relevant to field experiments. Our work supports more effective use of
27 acoustic data for permafrost monitoring and highlights the importance of considering both ice

28 saturation and microstructural characteristics when assessing the acoustic properties of ice-
29 bearing sediment.

30

31

INTRODUCTION

32 The elastic properties of ice-bearing sand are of great interest in both geotechnical
33 engineering and environmental science, particularly in permafrost settings (e.g., Bustamante et
34 al., 2023; Kang et al., 2021; Oswell, 2011). Permafrost, or permanently frozen ground, is a
35 critical component of the cryosphere, impacting infrastructure stability (e.g., Hjort et al., 2018)
36 and global climate dynamics (e.g., Schuur et al., 2015). In a warming climate, methane
37 emissions from permafrost degradation are expected to rise (Meredith et al., 2022). In order to
38 monitor and address these environmental challenges, it is important to be able to link elastic
39 wave properties to ice content (Hilbich et al., 2022).

40 Elastic wave velocity and attenuation vary with frequency, and this variation affects the
41 interpretation of seismic survey and sonic log data, as well as data generated by laboratory
42 experiments. Elastic properties are also sensitive to pore fluid composition and content (e.g.,
43 Emerson and Foray, 2006; Rubino and Holliger, 2012; Sutiyoso et al., 2024) and to the state of
44 stress as represented by confining and pore pressures (Alkire and Andersland, 1973; Falcon-
45 Suarez et al., 2019). Understanding these dependences is therefore essential for comparison of
46 elastic property data from different types of experiment (Kolsky, 1964). Most laboratory studies
47 are conducted at ultrasonic frequencies (150 kHz to 1 MHz; e.g., Dou et al., 2016; Li and
48 Matsushima, 2024; Matsushima et al., 2016) that differ greatly from those of field
49 measurements. To fill this gap, further research is needed at frequencies closer to those of field
50 measurements, such as sonic frequencies used in borehole logging.

51 Laboratory data serve to validate and enhance rock physics models that predict how ice
52 saturation, distribution, and morphology in porous media influence the mechanical and acoustic
53 properties of ice-bearing sediments (e.g., Li and Matsushima, 2024; Matsushima et al., 2016).
54 A terminology first introduced by Dvorkin et al. (1999) for high-porosity ocean-bottom

55 sediments and later adapted for gas hydrates by Helgerud et al. (1999), ice morphologies are
56 categorized into non-cementing and cementing types based on their interaction with the
57 sediment matrix. In non-cementing morphology, ice does not bond to the sediment framework.
58 Within this category, pore-floating ice grows freely in pore spaces without connecting grains,
59 while pore-bridging ice physically spans the spaces between adjacent grains and may contribute
60 to frame support (Hu et al., 2014; Priest et al., 2009). In contrast, cementing morphology
61 involves ice that bonds directly to sediment grains, either at grain contacts (contact cementing)
62 or as a coating around grains (grain coating) (Best et al., 2013; Ecker et al., 1998; Helgerud et
63 al., 1999). Cementing morphologies enhance load-bearing capacity, significantly influencing
64 the elastic properties of sediment. The concept of morphology is applied in several existing
65 rock physics models, including those based on Biot's (1956a, 1956b) theory. Such models may
66 consider two phases (sediment and pore fluid) or three phases (sediment, ice or hydrate, and
67 pore fluid; e.g., Leclaire et al., 1994; Marín-Moreno et al., 2017). Because ice-bearing and
68 hydrate-bearing sediments share similar physical properties, models developed for one system
69 are often applicable to the other (Helgerud et al., 1999), providing a framework for predicting
70 elastic wave behavior in frozen and partially frozen media.

71 Permafrost can extend up to 365 m below the surface (Dobiński, 2020) with estimated
72 confining pressures ranging from 4.9 to 6.2 MPa (Kawasaki et al., 1983). Hence, effective
73 monitoring and interpretation of permafrost environments requires an understanding of the
74 combined effect of ice saturation, distribution, and morphology and of pressure changes on
75 seismic wave propagation at a given frequency. Here, we investigate the acoustic wave
76 properties of ice-bearing sands at different pressures within the sonic frequency range (1-20
77 kHz). The acoustic pulse tube setup and methodology described by Sutiyoso et al. (2025) were
78 applied to extend a dataset at 2.5 MPa effective pressure to two additional effective pressures
79 of 5.0 and 7.5 MPa. We assess our experimental results using three-phase rock physics models
80 to provide new insights into ice content estimates from seismic or sonic log data at in situ
81 pressures of typical permafrost formations.

82

83

MATERIALS AND METHODS

84 Ice-bearing sand sample

85 We used clay-free Leighton Buzzard sand with a mean grain diameter of 100 μm ,
86 chosen for its similarity to the grain size of typical permafrost sands (e.g., Fuchs et al., 2018;
87 Liu et al., 2023; Strauss et al., 2012). The sand was packed in a 0.5 m long PVC pipe and sealed
88 with PVC endcaps to enable uniform confining pressure. The acoustic impedance of the PVC
89 material is $2.9 \times 10^6 \text{ kg m}^{-2} \text{ s}^{-1}$ (Selfridge, 1985), while the impedance of the sand pack ranges
90 from 2.2 to $6.8 \times 10^6 \text{ kg m}^{-2} \text{ s}^{-1}$, depending on whether it is water-saturated or ice-bearing (Kang
91 et al., 2021; Schumann et al., 2014; Sutiyoso et al., 2025).

92 To prepare the sample, we poured sand into the PVC pipe, compacting it in layers for
93 even compaction and scratching the surface between layers to minimize impedance contrasts.
94 The porosity of the sand pack was $41 \pm 0.1\%$, calculated from the wet-dry mass balance, with
95 uncertainties determined through error propagation. Once compacted, we gradually added a
96 pre-calculated amount of de-ionized water and tapped the pipe to release air bubbles. This
97 process helped in reducing gas bubbles in the ice, resulting in more consistent laboratory
98 measurements (McCutchan and Johnson, 2022). After fully saturating the sample, we sealed it
99 and let the water distribute for 24 hours. Although the sample was saturated, this step helped to
100 balance pore pressure and promote more uniform water distribution across the packed layers
101 through slow internal movement driven by gravity and capillary forces (Snehota et al., 2015).
102 Then, we froze the sample at -10°C for 48 hours. Further details about the sample preparation
103 can be found in Appendix A.

104 Ice saturation (S_i) was inferred from the elapsed melting time during measurements. We
105 established a baseline by measuring velocity and attenuation in the fully melted state ($S_i = 0$).
106 The initial ice saturation was assumed to be $S_i = 1$, although some unfrozen water likely
107 remained in thin films around the grains (Watanabe and Mizoguchi, 2002). Due to the time
108 needed to reach the target pressure inside the pulse tube after transfer of the sample from the

109 chest freezer, measurements at full ice saturation were not possible, so a regression model was
110 used to estimate velocity and attenuation at $S_i = 1$. Ice saturation was calculated using an
111 empirical relationship, $S_i = 1 - \left(\frac{t}{T}\right)^n$, where t is the time elapsed during measurement (in
112 seconds), T is the total time for complete melting (determined by the velocity and attenuation
113 at the fully melted state), and n is an empirical parameter describing the exponential relationship
114 between ice melting and time. The parameter n was derived by comparing experimental results
115 with rock physics models and minimizing an objective function. Additional details on the ice
116 saturation estimation are provided in Appendix B.

117 Note that the volumetric expansion of ice might have introduced errors in saturation
118 estimation (French, 2007), along with the potential unfrozen water in the form of thin films
119 (Dash et al., 1995; Watanabe and Mizoguchi, 2002). To account for these uncertainties, we
120 have included error bars in our figures, based on a conservative 9% error estimate that considers
121 these sources of error (French, 2007).

122

123 **Pulse tube measurements**

124 We measured velocity and attenuation (inverse quality factor, $1/Q$) using a 4.5-meter-
125 long acoustic pulse tube with variable-frequency chirp signals within the range of 1-20 kHz.
126 The tube uses a piezoelectric transducer located at the base of a stainless-steel cylinder filled
127 with water to propagate plane waves along the tube's axis, based on an acoustic waveguide
128 concept (Redwood, 1960). The sand-ice sample was suspended in the water-filled tube about
129 halfway down. We collected new acoustic measurements at effective pressures (P_{eff}) of 5.0 and
130 7.5 MPa under a controlled temperature of 19°C, and included previously reported data at 2.5
131 MPa (from Sutiyoso et al., 2025). Assuming a permafrost density of 1700 kg m⁻³ (Kawasaki et
132 al., 1983), our experiments simulated conditions similar to those of thawing permafrost at
133 depths of approximately 150 – 450 m. While permafrost has been reported to extend to depths
134 of up to 365 m (Dobiński, 2020), a higher-pressure limit was selected to account for variability

135 in permafrost density and to provide a conservative upper bound. Our temperature setting
136 reflects an extreme surface warming scenario (Kim et al., 2024).

137 At each effective pressure, we allowed the sample to thaw during the measurement
138 process, enabling us to track changes in acoustic wave properties as the ice gradually melted.
139 After completing the measurements at one pressure, the sample was removed from the pulse
140 tube and rested for 24 hours at atmospheric pressure to reduce residual effects from compression
141 under confining pressure, then re-frozen inside a chest freezer to restore the initial frozen
142 condition before moving to the next pressure step. Although this method freezes the sample
143 before applying pressure, unlike natural permafrost, which freezes gradually under stress, it
144 provides controlled conditions to isolate pressure effects on acoustic properties. Our
145 measurements covered the full melting process, from frozen to completely thawed states. This
146 experimental approach ensures the results remain applicable to a wide range of natural
147 permafrost conditions, including regions with thick permafrost or elevated overburden stress.

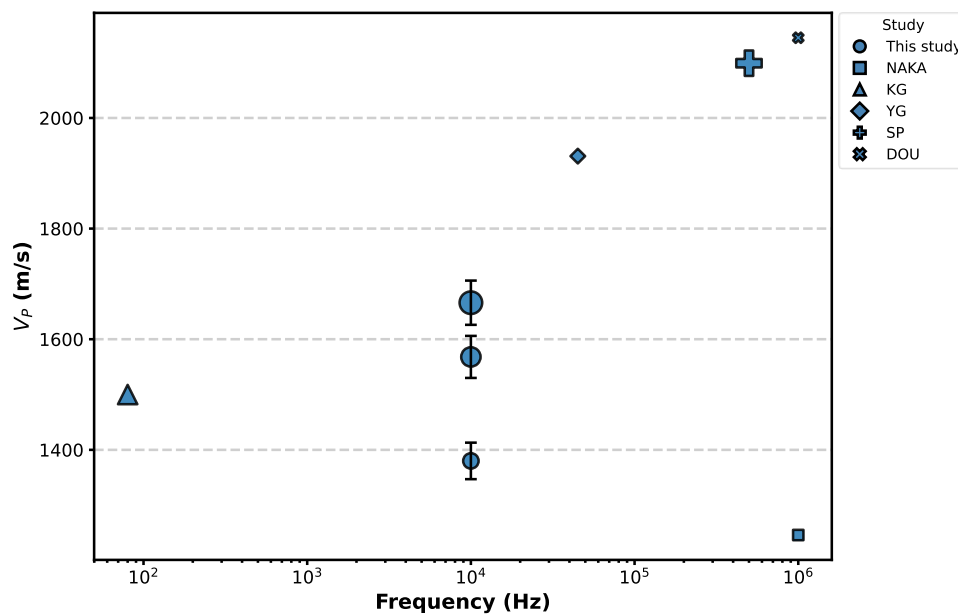
148 For each measurement, we recorded signal amplitude as voltage across the ice saturation
149 stages. We applied a Fast Fourier Transform to deconvolve the raw signals and obtain the
150 impulse response, followed by time-domain gating to eliminate extraneous reflections. Then,
151 we applied a non-linear inversion model incorporating the scattering matrix method to
152 determine the complex velocity, and attenuation was derived according to Equation 1 (Mavko
153 et al., 2009). The inversion incorporated reference (sample-less) pulse tube measurements to
154 eliminate transducer transfer functions and temperature dependency.

$$Q^{-1} = \frac{1 - e^{-2\pi \frac{v_1}{v_2}}}{2\pi} \quad (1)$$

155 where V_1 and V_2 are the real and imaginary velocities, respectively.

156 The pulse tube was calibrated by comparing experimental measurements with
157 theoretical transmission coefficients to determine velocity and attenuation errors, following the
158 method of McCann et al. (2014). The relative experimental uncertainties were $\pm 2.4\%$ for
159 velocity and $\pm 5.8\%$ for attenuation. Calibration measurements using a nylon rod also agreed
160 with ultrasonic data extrapolated to the sonic range using a standard linear solid model (Kolsky,

161 1964), with less than $\pm 1\%$ difference. Figure 1 compares the compressional velocity measured
 162 in this study with published values for similar sand packs. Our velocities are comparable with
 163 lower-frequency measurements (e.g., Kang et al. (2021) at seismic frequencies), and are lower
 164 than those measured at ultrasonic frequencies (Dou et al., 2016; Spangenberg et al., 2018; Yang
 165 et al., 2021). Nakano and Arnold (1973) reported measurements on saturated Ottawa sand with
 166 a grain size of 1 mm (about ten times larger than in our samples), which explains their slightly
 167 lower velocity. Overall, these comparisons demonstrate that our results are within a reasonable
 168 range of published data, given differences in measurement frequency and experimental design.
 169 Figure 2 presents the schematic diagrams of the pulse tube and examples of measured and
 170 deconvolved signals. Further details of the experimental setup and data processing are given by
 171 North and Best (2015) and Sutyoso (2025).



172
 173 **Figure 1** Comparison of compressional velocity (V_p) of water-saturated sand measured in this
 174 study with values reported in published studies. The three data points for this study represent
 175 measurements at different effective pressures (2.5, 5.0, and 7.5 MPa), with error bars indicating
 176 experimental uncertainty. Marker size represents the confining pressure, ranging from
 177 atmospheric pressure to 10 MPa. The study codes are as follows: KG (Kang et al., 2021), YG
 178 (Yang et al., 2021), SP (Spangenberg et al., 2018), DOU (Dou et al., 2016), and NAKA (Nakano
 179 and Arnold, 1973).

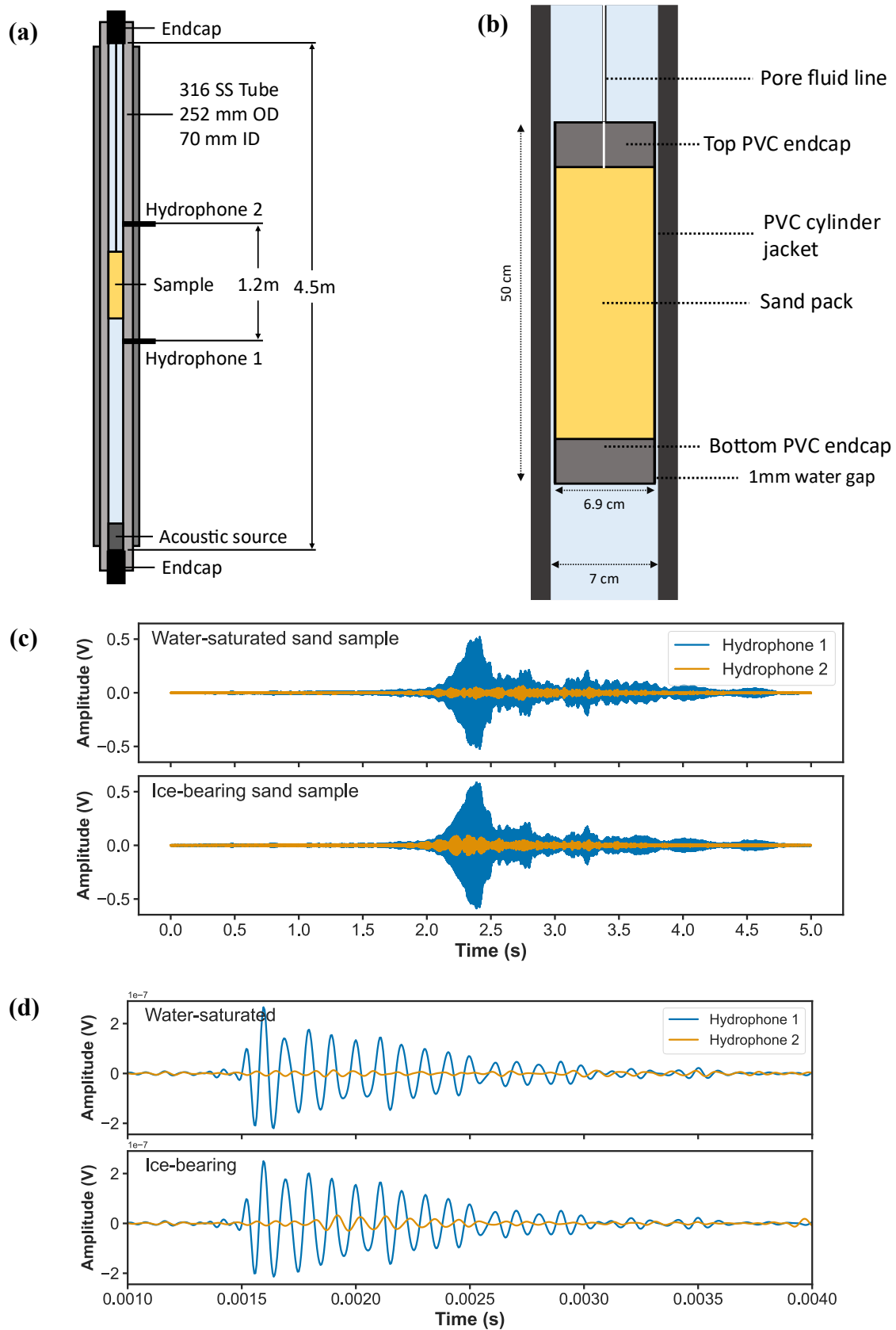


Figure 2 Experimental apparatus and resulting raw and processed data: (a) Schematic diagram of the pulse tube with dimensions; (b) details of the PVC-jacketed sample inside the water-filled pulse tube; (c) raw time-series signals acquired during measurements; (d) deconvolved signals for water-saturated and ice-bearing sand samples on both hydrophones (see panel (a) for hydrophone positions).

181 To ensure accurate measurements, we determined cut-off frequencies based on the
182 requirement that at least half of the wavelength should propagate through the 0.5-meter-long
183 sample, with wavelengths calculated as velocity divided by frequency. The corresponding cut-
184 off frequencies are 4.0 kHz for $P_{eff} = 2.5$ MPa and 4.8 kHz for the 5 and 7.5 MPa data,
185 respectively, resulting in half-wavelengths of 0.41 - 0.50 m. Below these frequencies, the half-
186 wavelengths exceed the sample length, and thus may not fully represent the bulk sample
187 conditions. Aside from frequency dependence analysis, we mainly focus on the experimental
188 results at 10 kHz, the mid-bandwidth frequency. Nevertheless, data below the cut-off are still
189 shown because they provide useful context for frequency-dependent trends and help identify
190 the onset of reliable wave propagation within the measurement band.

191

192 **Rock physics models**

193 We used two rock physics models incorporating Biot's theory to investigate the
194 mechanisms underlying the melting process in ice-bearing sand. The first, developed by
195 Leclaire et al. (1994), extends Biot's (1956a, 1956b) theory to predict elastic wave behavior in
196 frozen media comprising sediment matrix, ice, and unfrozen water. This model assumes that a
197 thin film of water around the grains prevents direct contact between the sediment and ice, except
198 in fully frozen conditions. The second model involves substituting hydrate with ice in the
199 hydrate-bearing effective sediment (HBES) model (Marín-Moreno et al., 2017), which then
200 treats pore-filling ice as part of the pore fluid and cementing ice as part of the sediment frame.
201 In both models, the elastic moduli of the sediment frame vary with effective pressure. In the
202 HBES model, this variation follows the Hertz-Mindlin contact theory (Mindlin, 1949). In
203 Leclaire et al.'s (1994) model, it follows Biot's theory. Thus, the models explicitly account for
204 the influence of effective pressure on both velocity and attenuation.

205 We extended the HBES model by incorporating additional effective medium
206 approximations by Brie et al. (1995) and Voigt (1889), alongside the existing Reuss (1929)
207 approximation, to calculate pore fluid bulk moduli and assess how ice distribution (whether

208 uniform or patchy) affects acoustic properties. We also investigated the effect of ice
 209 morphology on acoustic velocity and attenuation, defined by the proportion of pore-filling (PF)
 210 and cementing ice ($C = 1 - PF$). The HBES model treats cementing ice as part of the sediment
 211 frame, using the Voigt-Reuss-Hill average for bulk and shear moduli, as described by Ecker et
 212 al. (2000). In contrast to the classic approach of Dvorkin et al. (1999) and Helgerud et al. (1999),
 213 in which cementing ice replaces sand grains in the matrix, the HBES model preserves this
 214 matrix and incorporates a distinction between cementing ice coating or bonding at grain
 215 contacts. Unlike gas hydrate, ice lacks microporosity, which is pores smaller than a micron that
 216 drives squirt-flow. Therefore, it contributes less to stress-induced attenuation (Best et al., 2013).
 217 Thus, we consider the pore-filling and cementing morphologies sufficient to capture the
 218 underlying mechanisms controlling acoustic parameters in ice-bearing sediments. The model
 219 inputs are provided in Table 1.

220

221 *Table 1 Fixed input parameters that are used in all model runs and case-dependent parameters*
 222 *that are used only in HBES model runs.*

Parameter	Value	Units	Reference
Fixed input parameters			
Experimental conditions			
Effective pressure (P_{eff})	2.5, 5.0, 7.5	MPa	
Temperature	19	°C	
Sand sediment properties			
Porosity without ice	0.41		Measured
Critical porosity	0.38		Best et al. (2013)
Sand grain bulk modulus	36×10^9	Pa	Simmons (1965)
Sand grain shear modulus	45×10^9	Pa	Simmons (1965)
Sand grain density	2650	Kg m^{-3}	Simmons (1965)
Sand grain diameter	10^{-4}	m	Best et al. (2013)
Coordination number	9		Murphy (1982)
Tortuosity	3		Berryman (1981)
Ice grain properties			
Ice bulk modulus	5.5×10^9	Pa	Chang et al. (2021)
Ice shear modulus	2.7×10^9	Pa	Chang et al. (2021)
Case-dependent input parameters			
Pore-filling saturation	0.6 – 1.0		
Sand column permeability	0.3 – 1.1	Darcy	

223

RESULTS

224

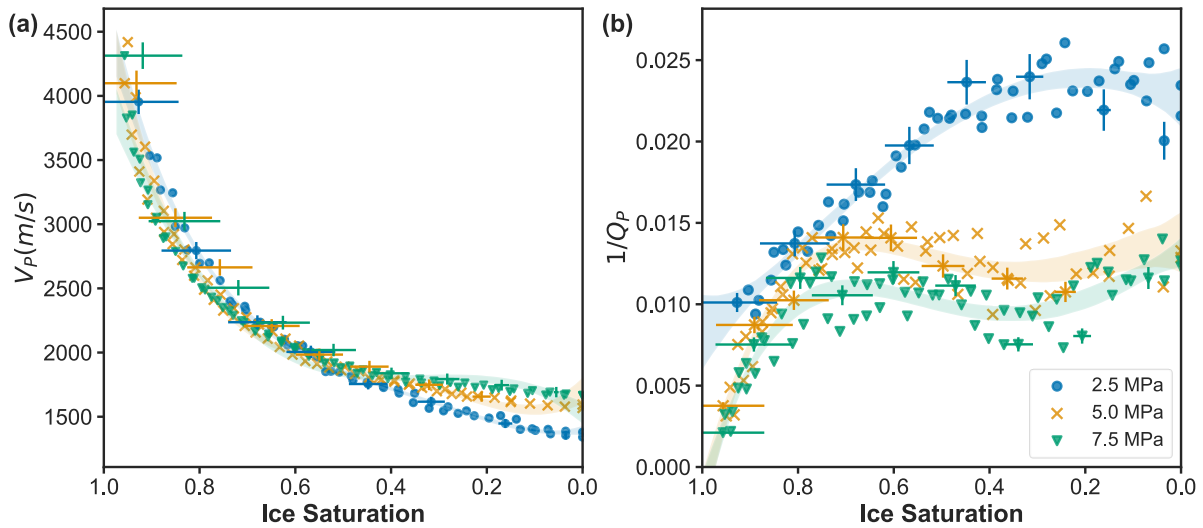
225 Experimental results

226 Figure 3 shows the evolution of the elastic wave attributes (velocity, V_P and attenuation,
227 I/Q_P), for the whole ice saturation (S_i) range at a frequency of 10 kHz and is representative of
228 the behavior at other frequencies measured. Velocity decreases as ice saturation decreases
229 across all effective pressure (P_{eff}) conditions (Figure 3a). The slope of the curve is steeper in
230 the ice saturation range $S_i > 0.5$, and the change of V_P with S_i within this S_i range is 20% larger
231 at 2.5 MPa than at 7.5 MPa. At high ice saturation ($S_i > 0.9$), velocities at P_{eff} of 2.5 and 5 MPa
232 are comparable and slightly higher than at 7.5 MPa by ~ 300 m/s. At zero saturation ($S_i = 0$),
233 velocity is highest at 7.5 MPa, followed by 5 MPa and 2.5 MPa, as expected for water-saturated
234 sand packs (Zimmer et al., 2002). The overall velocity drop from high to zero saturation is
235 largest at 2.5 MPa (~ 3000 m/s) and smaller at 5 MPa and 7.5 MPa (~ 2500 m/s), suggesting that
236 ice content exerts a stronger influence on the elastic properties at lower pressure.

237 Attenuation increases as ice melts from maximum saturation to $S_i \sim 0.2$ at 2.5 MPa, and
238 to $S_i \sim 0.7$ at 5 and 7.5 MPa, after which it remains relatively constant down to $S_i = 0$ across all
239 pressures (Figure 3b). The saturation corresponding to attenuation peak increases by ~ 0.5 with
240 increasing effective pressure. This observation suggests that at higher effective pressure, the
241 sand grains are more compact due to closer grain contact, making the sand matrix more resistant
242 to deformation as the ice melts (Zimmer, 2003).

243 Across ice saturation levels, the 2.5 MPa data consistently show the highest attenuation,
244 followed by the 5 and 7.5 MPa data. At $S_i > 0.7$, attenuation values are similar across all
245 pressures, within the range of data variability. However, as the ice melts, attenuation becomes
246 more sensitive to pressure, with a maximum variation of ~ 0.015 at $S_i \sim 0.3$. The slope of the
247 attenuation curve steepens more as ice melts at $P_{eff} = 2.5$ MPa and less for the 5 and 7.5 MPa
248 cases, similar to the behavior of the velocity curves.

249



250

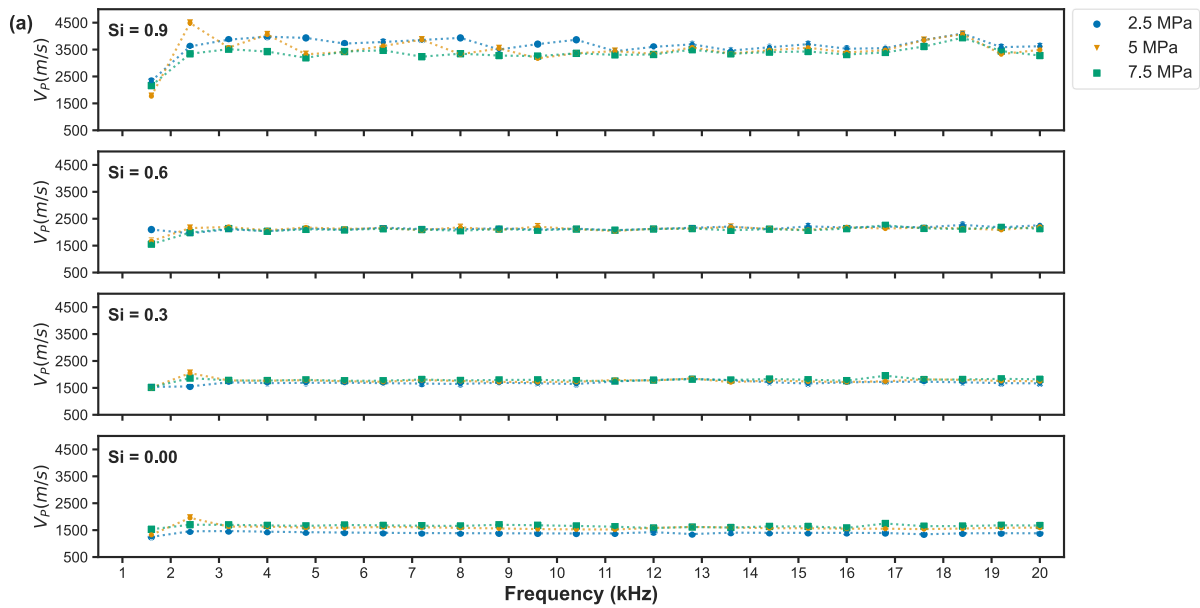
251 **Figure 3** Variations in P-wave velocity (V_P) and attenuation ($1/Q_P$) at 10 kHz during the ice
 252 melting process at various effective pressures, with shaded areas representing fourth-order
 253 polynomial regression models with a confidence interval of 90% (R^2 of 0.99, 0.98, 0.98 for
 254 velocity and 0.94, 0.82, 0.79 for attenuation at 2.5, 5, and 7.5 MPa, respectively). Error bars
 255 are plotted every 10 data points.

256

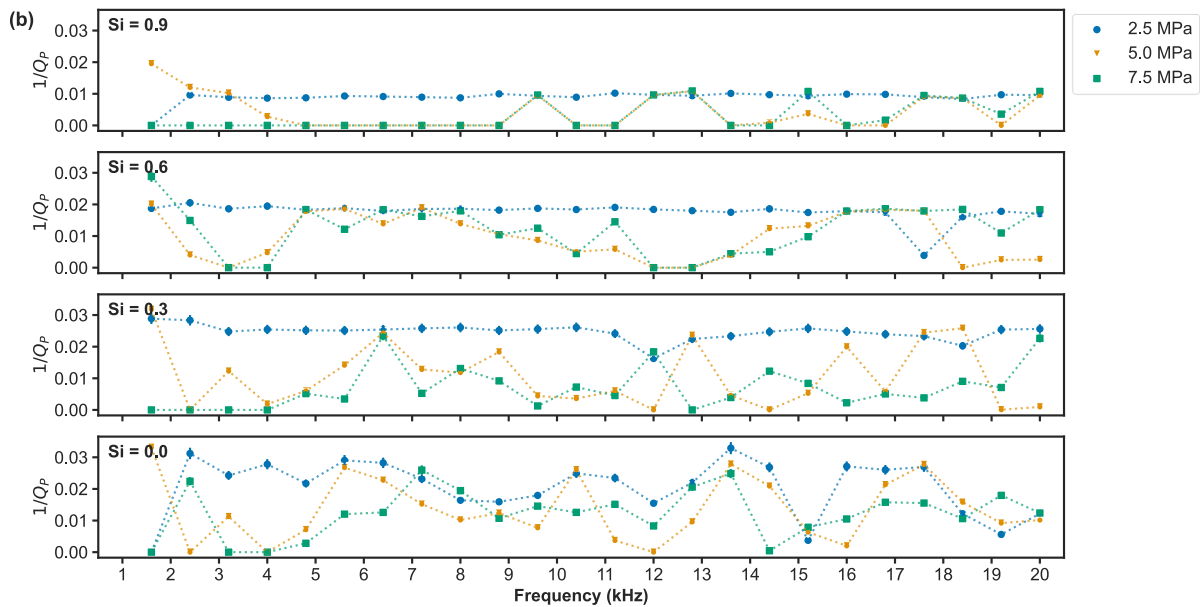
257 Velocity varies slightly with frequency, showing similar maxima at ~ 18 kHz and $S_i =$
 258 0.9 for all three pressures (Figure 4a). These maxima could be related to ice redistribution
 259 during early melting that results in changes at cm-scale, given the wavelength of 0.1 m at that
 260 frequency. At high ice saturations (mainly $S_i > 0.9$), velocity generally decreases with
 261 increasing frequency, whereas at intermediate saturations ($S_i \sim 0.6-0.9$), velocity tends to
 262 increase with frequency, with some dependence on pressure (Figure 5). These contrasting trends
 263 indicate that the dominant controls on frequency-dependent velocity evolve as the pore structure
 264 transitions from ice-dominated to increasingly water-connected during thawing. This transition
 265 may reflect the squirt-flow type behavior as thawing produces partially connected fluid
 266 pathways, altering the pore-scale pressure equilibration at higher frequencies (Müller et al.,
 267 2010).

268 Attenuation shows the same trend with frequency as with velocity at low P_{eff} (2.5 MPa),
 269 except at $S_i = 0$. When P_{eff} increases, attenuation shows complex patterns for the whole
 270 frequency range (Figure 4b). This frequency sensitivity may relate to the squirt flow processes
 271 as suggested above, because partially connected water pockets could also increase energy loss

272 at specific frequencies (Carcione et al., 2003). However, the variability observed in the trends
 273 for different pressures suggests that stress-induced mechanical phenomena at the grain scale
 274 also affect pore connectivity. At $S_i = 0$, attenuation varies similarly above 5 kHz across all
 275 pressures, with peaks around 13 - 14 kHz. These variations at higher frequencies may be
 276 influenced by small-scale heterogeneities, also seen in the velocity data.
 277

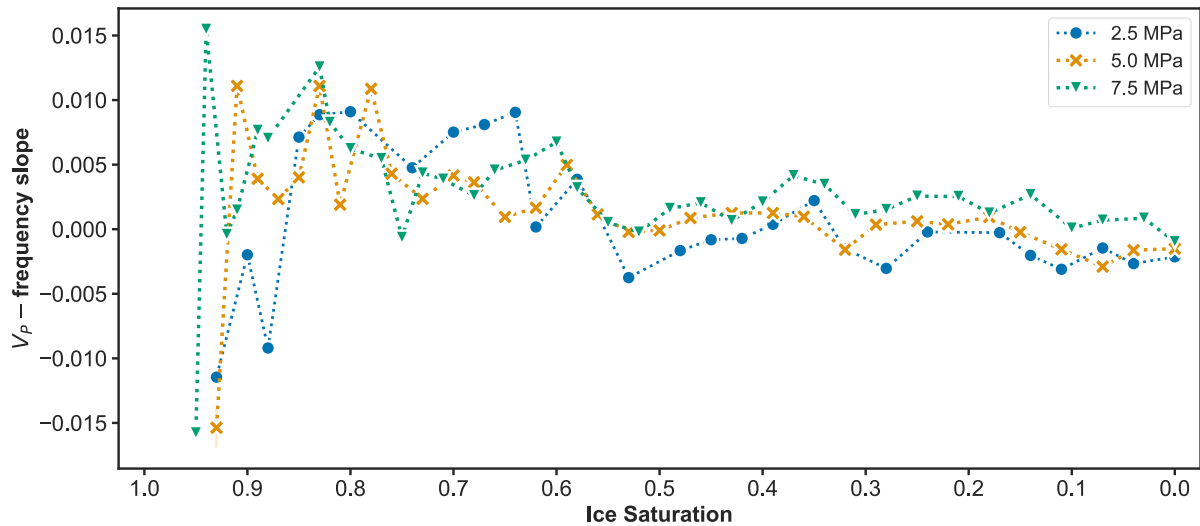


278



279

280 **Figure 4** Experimental results: a) P -wave velocity (V_P) and b) attenuation ($1/Q_P$) spectra at
 281 selected ice saturations (S_i). The error bars are smaller than the symbol sizes. Legends represent
 282 effective pressures in megapascals (MPa).



283

284 **Figure 5** Regression slope of P-wave velocity (V_P) versus frequency between the cut-off and
 285 maximum (20 kHz) frequencies as a function of ice saturations and effective pressures. Positive
 286 slopes indicate velocity increasing with frequency, while negative slopes indicate velocity
 287 decreasing with frequency. Legends represent effective pressures in megapascals (MPa).

288

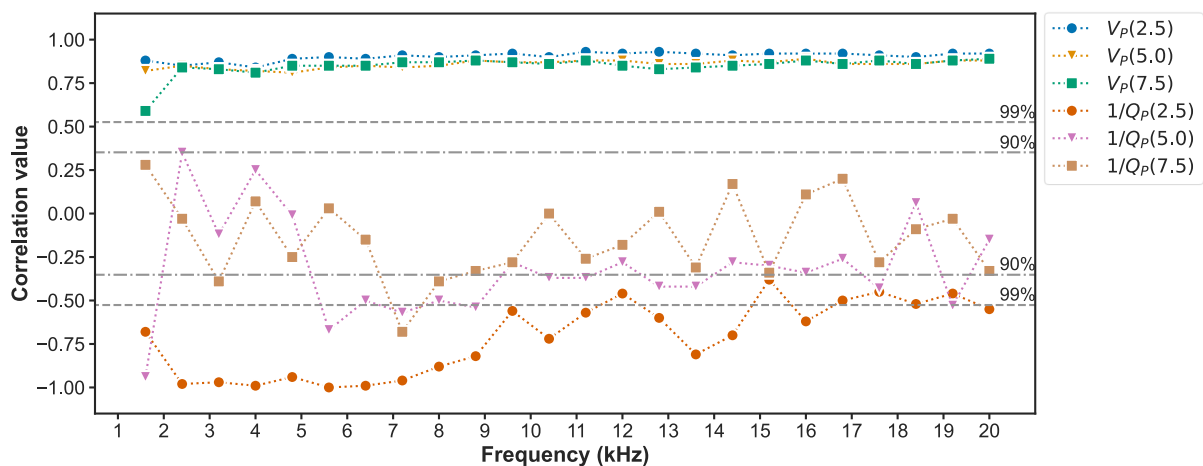
289 We also evaluated the relationship between the acoustic parameters and ice saturation
 290 at each frequency using Spearman's rank correlation (Figure 6). Specifically, we calculated the
 291 correlation coefficients between measured velocity or attenuation values and corresponding ice
 292 saturation levels across all saturations at each frequency. This analysis evaluates the sensitivity
 293 of each frequency's acoustic response to changes in ice saturation, leveraging the multi-
 294 frequency capability of the acoustic pulse tube. Velocity correlates strongly with changes in ice
 295 saturation ($r > 0.81$), consistently exceeding the 99% confidence level across all frequencies
 296 and effective pressures. As ice saturation decreases, velocity also decreases, as confirmed by
 297 the positive correlation.

298 In contrast, attenuation shows more complex behavior than velocity, and its relationship
 299 with ice saturation is not strictly monotonic (Figure 3b). For this reason, the correlation analysis
 300 is not intended to quantify a physical trend with saturation but rather to identify the frequency
 301 bands where attenuation responds most consistently to changes in ice content. At 2.5 MPa,
 302 attenuation has larger correlation magnitudes and lower measurement uncertainty, producing
 303 stronger correlations than at 5 and 7.5 MPa, where values are closer to the detection limit and
 304 uncertainties increase. The most robust correlations occur between 5 and 10 kHz, particularly

305 near 7 kHz, indicating that this band provides the clearest and most stable attenuation signal
 306 across pressures. These results may highlight the 5-10 kHz band as the most effective range for
 307 monitoring attenuation changes in the thawing of ice-bearing unconsolidated sediments, but
 308 they also point to limitations at higher pressures where attenuation becomes very small.

309 At higher pressures and lower ice saturations (5.0 and 7.5 MPa), attenuation values
 310 occasionally approached the system's detection limit (<0.01 or $Q > 100$), potentially masking
 311 subtle changes in wave-induced fluid flow or permeability. The lower limit for detectable
 312 attenuation within our sample arises from the departure from the plane-wave propagation
 313 assumed in the data-inversion algorithm. This behavior can also contribute to apparent
 314 deviations from the Kramers–Kronig causality principle, which may be amplified by the finite
 315 frequency bandwidth of laboratory measurements (Mobley et al., 2000). Despite these
 316 limitations, the overall trends remain physically consistent with Biot-type behavior and are
 317 relevant for geophysical monitoring, particularly in lower-pressure or higher-saturation settings
 318 where Biot flow is more active, as attenuation magnitudes above 0.01 are of practical
 319 importance (e.g., Allmark et al., 2018; Parolai et al., 2022).

320



321

322 **Figure 6** Spearman's rank correlation coefficients between acoustic properties (P-wave
 323 velocity, V_P and attenuation, $1/Q_P$) and ice saturation, calculated at each frequency and
 324 effective pressure (in megapascals). The vertical axis ranges from -1 to $+1$ to accommodate
 325 both positive (typically for velocity) and negative (typically for attenuation) correlations. The
 326 90% and 99% confidence level lines apply to both acoustic properties and indicate statistically
 327 significant correlations.

328

329 **Insight from modeling**

330 Initially, we compared our data to the LeClaire model and to HBES models with entirely
331 pore-filling ice and a permeability of 0.5 D (Fig. 7a). All models predict that velocity decreases
332 with varying rates when ice melts. The LeClaire model predicts the steepest decrease at high
333 saturations ($S_i > 0.8$), followed by the HBES models with Voigt, Brie, and Reuss
334 approximations. These differences reflect the influence of assumed ice distribution on velocity,
335 since the LeClaire model assumes the most heterogeneous (patchy) distribution, while HBES-
336 Reuss represents the most uniform, with Voigt and Brie in between.

337 At $P_{eff} = 2.5$ MPa, the experimental velocities align well with the HBES-Voigt model,
338 particularly at intermediate saturations ($S_i = 0.8$ to 0.4), but shift towards the LeClaire model at
339 lower saturations ($S_i < 0.2$). At 5 and 7.5 MPa, experimental velocities are still in good
340 agreement with HBES-Voigt at most saturations but are closer to the LeClaire model than at 2.5
341 MPa.

342 Higher effective pressure causes experimental velocities to fit closer to the LeClaire
343 prediction at intermediate saturations (e.g., $S_i = 0.8$ to 0.4), likely due to pressure-induced
344 changes in pore structure (Zimmer et al., 2002). As grain contact increases under higher
345 pressure, ice in smaller pore spaces may melt at different rates compared to larger spaces, where
346 the availability of pore fluid for heat transfer differs, promoting uneven melting rates (Abbasi
347 et al., 2022; De Lemos, 2012).

348 All modeled attenuations increase with melting, although the trends are less
349 straightforward than for velocities (Figure 7b). At 5 and 7.5 MPa, attenuation increases from S_i
350 = 1.0 to ~0.4, then levels off or decreases. At 2.5 MPa, similar patterns only occur in the LeClaire
351 and HBES-Voigt models, while the HBES-Brie and Reuss models show near-continuous
352 increases. While ice distribution affects velocity at all pressures, attenuation becomes less
353 sensitive to distribution at higher pressures in the HBES models. We also observed shifts in the
354 modeled attenuation peaks, although these differed from the experimental trends. For example,

355 the HBES-Voigt peak shifts from lower to higher ice saturation as effective pressure increases,
356 moving from $S_i = 0.125$ at 2.5 MPa to $S_i = 0.375$ at 7.5 MPa.

357 At 2.5 MPa, the measured attenuation aligns well with the HBES-Voigt model at $S_i <$
358 0.6 but exceeds the predictions of this model at higher saturations, possibly indicating an
359 additional loss mechanism beyond Biot theory. At 5 and 7.5 MPa, the experimental trends
360 become more complex. Measured attenuation is higher than predicted at $S_i > 0.6$, and more
361 variable at lower saturations, but still closer to the HBES models than to the Leclaire model.

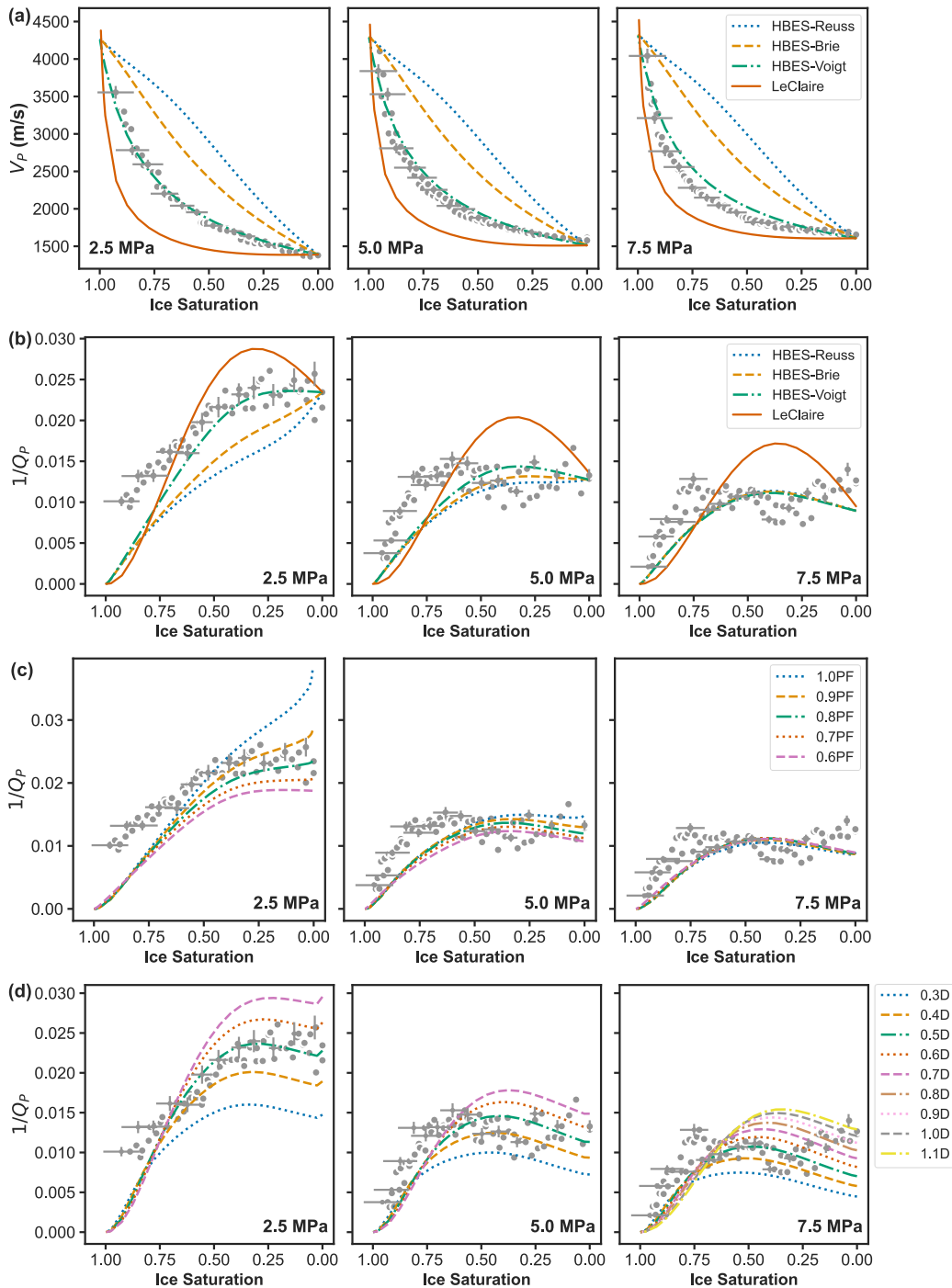
362 We then investigated the effects of ice morphology and sediment frame permeability
363 using the HBES-Voigt model, which showed the best fit to experimental data. The following
364 discussion focuses on attenuation, as velocity does not change significantly with either
365 parameter (see Appendix B). Modeled attenuation increases with pore-filling (*PF*) saturation
366 across all saturations and pressures (Figure 7c). This effect is strongest at 2.5 MPa, especially
367 at low ice saturations ($S_i < 0.4$). Measured attenuation aligns well with the higher PF saturation
368 curves at low ice saturations ($S_i < 0.6$), suggesting a transition from cementing ($C = 1 - PF$) at
369 higher saturation to pore-filling at lower saturations. This trend is less pronounced at higher
370 pressures. These variations offer insight into how acoustic properties are affected by melting,
371 particularly at lower ice saturations where the formation is potentially less uniform.

372 Modeled attenuation also varies with permeability at most ice saturations ($S_i < 0.8$)
373 across all pressures (Figure 7d). Higher permeability leads to higher attenuation, especially at
374 low saturation ($S_i < 0.4$), consistent with Biot's global flow theory, where greater relative
375 motion between the solid matrix and viscous fluid leads to higher attenuation. Measured
376 attenuation mostly corresponds to model permeabilities of 0.3 - 0.6 D. These values are
377 reasonable for tightly packed ice-bearing sand in permafrost conditions, where values of around
378 0.01 - 1.01 D are reported by Sizemore and Mellon, 2008). The increase in permeability may
379 explain the distinct increase in measured attenuation at lower ice saturation ($S_i < 0.3$), especially
380 at 7.5 MPa. As ice melts, liquid water content and permeability increase due to more spaces

381 becoming available (Mahabadi et al., 2019), thus allowing greater pore fluid movement relative
 382 to solid grains, which consequently increases attenuation (Lee et al., 2024).

383

384



385

386

387

388

389

390

391

392

393

394

Figure 7 Comparison of experimental data and model results for P-waves at 10 kHz: a) velocity (V_P) and b) attenuation ($1/Q_P$). In the HBES models, the pore-filling saturation PF is 1.0 and the permeability is 0.5 D; c) attenuation at different PF (with the remainder of S_i as cementing ice, i.e., $1 - PF$); and d) attenuation at different permeabilities for $PF = 1.0$. Results in c) and d) are modeled using the HBES model with Voigt approximation. Cross-error bars are plotted every 15 experimental data points.

DISCUSSION

395

396 Ice content in ice-bearing sand affects both acoustic velocity and attenuation across all
397 tested effective pressures. As ice melts, velocity decreases and attenuation increases, which is
398 consistent with previous studies at ultrasonic (e.g., Matsushima et al., 2016; Yang et al., 2021)
399 and sonic (Sutiyoso et al., 2025) frequencies. We found that ice saturation could mask the stress
400 effect within the measured range, as the V_P - S_i trends are similar across all effective pressures.
401 In contrast, attenuation is more pressure-dependent, especially at high ice saturations. At low
402 pressure, the sand may experience more strengthening from ice formation, thus losing more
403 structural support as the ice melts (i.e., decreasing frame bulk modulus), which affects both
404 velocity and attenuation even down to fully melted conditions ($S_i = 0$). These findings highlight
405 the value of conducting acoustic measurements in ice-bearing sediments at a variety of effective
406 pressures. At lower effective pressures, grain-to-grain contacts may be forced apart by ice-
407 induced expansion during crystallization (Alkire and Andersland, 1973). This effect is also
408 observed with gas hydrates (e.g., Priest et al., 2021). Because water expands upon freezing, ice
409 formation could dilate the sand pack at lower pressures, with grains settling back into contact
410 as the ice melts. In contrast, higher pressures may restore grain contact before melting, possibly
411 deforming any ice initially formed. As a result, ice melting exhibits the largest acoustic shift at
412 2.5 MPa. At higher pressures (5.0 and 7.5 MPa), stronger grain contacts diminish the influence
413 of ice in supporting the matrix during the melting process. In other words, acoustic propagation
414 is more influenced by ice-water interactions at lower pressures and by the sand frame-water
415 system at higher pressures.

416 Velocity data show an inflection point (where velocities under all effective pressures
417 intersect) at $S_i \sim 0.5$ (Figure 3). This observation may suggest that load-bearing ice is significant
418 for $S_i > 0.5$, which would strongly depend on the degree of dilation during the ice-forming stage.
419 Across pressures, attenuation at $S_i > \sim 0.8$ shows similar values, likely because Biot-type flow
420 is minimal due to pore-clogging effects, resulting in small but finite losses. Since ice is assumed
421 to be non-microporous, attenuation is essentially controlled by global Biot fluid flow, with

422 minimal contribution from sub-microporous squirt flow. Consequently, attenuation is largely
423 linked to permeability for a given ice saturation. In addition, attenuation would also reflect ice
424 morphology (e.g., Sahoo and Best, 2021), as ice transitions from a cementing or load-bearing
425 phase to a pore-filling morphology with decreasing saturation. This transition can influence
426 how Biot flow and frame stiffness evolve with pressure and melting. Therefore, attenuation
427 may serve as an indirect diagnostic of both ice saturation and morphology.

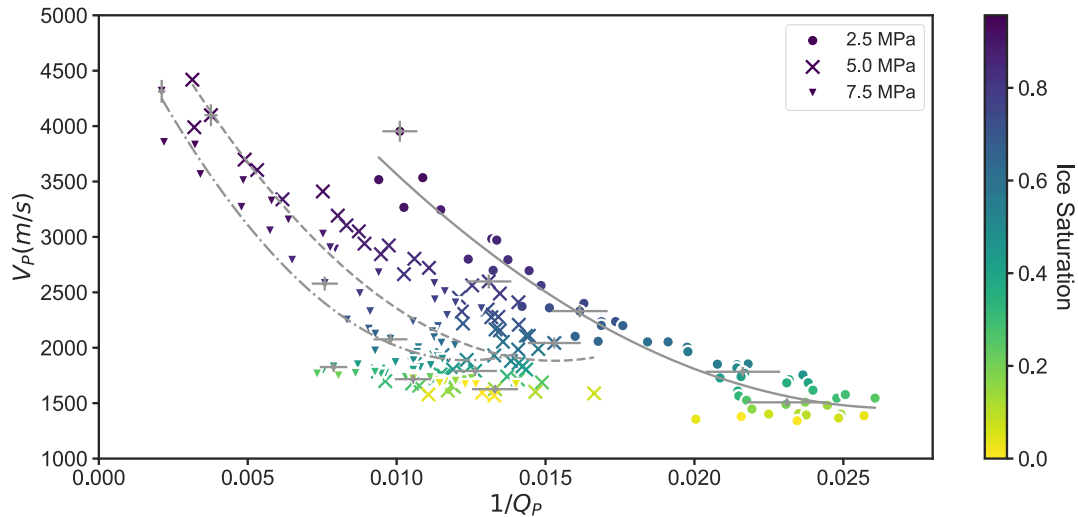
428 Scattering attenuation arising from small-scale heterogeneities, such as patchy ice
429 distribution, may also contribute to the observed acoustic response, particularly at intermediate
430 saturations where impedance contrasts are the highest (Hefner et al., 2006; Wu and Aki, 1985).
431 However, our measurements at sonic frequencies in a homogeneous sand pack suggest that
432 intrinsic attenuation remains dominant. Direct validation of ice structure (e.g., via micro-CT
433 imaging or thin section analysis) is not feasible due to the sample size and complex
434 configuration of our experimental setup. Nonetheless, the hydrate morphologies represented in
435 HBES have been validated with X-ray computer tomography (Sahoo et al., 2018), and ice is
436 widely recognized as an appropriate analogue for hydrate in this context (Helgerud et al., 2009;
437 Spangenberg et al., 2018), indirectly supporting our assumptions about ice distribution.

438 The inverse relationship between velocity and attenuation (Figure 8) across all effective
439 pressures is consistent with both model predictions and other experimental observations (e.g.,
440 Li and Matsushima, 2024; Yang et al., 2021). This effect results from matrix stiffening at high
441 ice saturations or high effective pressure, which allows acoustic waves to transmit more
442 efficiently, thereby reducing energy loss (Li and Matsushima, 2024; Zimmer et al., 2002). The
443 clear velocity-attenuation trends and good correlations observed for each pressure, even within
444 such a small effective pressure range, suggest that inferring ice saturation at given depths is
445 feasible provided that both P-wave velocity and attenuation can be measured.

446 Velocity strongly correlates with ice saturation across the entire frequency range (1-20
447 kHz), while attenuation correlates more strongly at lower frequencies, particularly around 7
448 kHz (Figure 6). This may be because attenuation at 7 kHz is higher than at adjacent frequencies,

449 making it more detectable by the pulse tube system and leading to a stronger and more reliable
450 correlation at that frequency. Variation at higher frequencies may also be attributed to the
451 heterogeneities of water and ice distribution caused by the thawing process. At these
452 frequencies, attenuation becomes more sensitive to changes in ice content because the shorter
453 wavelengths are comparable in scale to the heterogeneities, making them more apparent. In
454 contrast, at lower frequencies, the longer wavelengths average out these small-scale variations,
455 resulting in a smoother and more predictable relationship between attenuation and ice content
456 (Sutiyoso et al., 2025). In addition, phase-transition effects at ice-water-grain interfaces can
457 further influence acoustic properties (Li and Matsushima, 2024). During thawing at high ice
458 saturations, thin water films forming at grain contacts may soften the sediment matrix, leading
459 to a decrease in acoustic velocity and an increase in attenuation. While water vapor formation
460 is theoretically possible, the pressure in our experiments (2.5-7.5 MPa) prevents bulk vapor
461 generation (Wagner et al., 2011). Therefore, the observed changes in acoustic response are
462 likely dominated by the general effects of phase transition at ice-water-grain interfaces. These
463 complementary behaviors highlight the potential of velocity and attenuation as dual indicators
464 to estimate ice content in field scenarios, particularly in well-logging applications at similar
465 frequencies (Hearst and Nelson, 1985). Well logs have commonly been used to identify
466 permafrost layers (e.g., Desai and Moore, 1968; Osterkamp and Payne, 1981), and the findings
467 of this study could improve the interpretation of such data by providing a more physically
468 grounded basis for estimating ice saturation.

469 In summary, velocity strongly correlates with ice saturation across the frequency band,
470 while attenuation exhibits its strongest correlation at lower frequencies, particularly around 7
471 kHz. These results highlight the importance of selecting an appropriate frequency range to
472 effectively capture frequency-dependent mechanisms related to ice content in ice-bearing
473 sediments. Optimizing measurement frequencies improves our ability to monitor and predict
474 changes in frozen grounds, with broader applications for quantifying and monitoring ice content
475 in permafrost regions (e.g., Hilbich et al., 2022; Lin et al., 2018).



477

478 **Figure 8** Variations in P-wave velocity (V_P) and attenuation ($1/Q_P$) at 10 kHz plotted against
 479 each other, with lines representing second-order polynomial regression models with R^2 of 0.94,
 480 0.72, and 0.72 at 2.5, 5, and 7.5 MPa, respectively. Marker types represent different effective
 481 pressures as shown in the legend. Cross-error bars are plotted every 15 data points.

482

483 While this study tests a range of effective pressures, allowing for insights into multi-
 484 depth conditions (approximately 150 – 450 m below the surface, depending on sediment
 485 density), we acknowledge that our use of a homogenous sand pack may differ from field
 486 conditions, which typically feature variable grain sizes and lithologies. To control sample
 487 variability, the same sample was reused across freeze-thaw and re-pressurization cycles.
 488 Repeated thermal and mechanical loading may introduce cumulative effects, which we
 489 mitigated by allowing the sample to rest between measurements. Subtle impacts may still occur,
 490 including sand dilation under pressure, microstructural rearrangements, changes in grain
 491 contact bonding due to repeated ice formation, or minor changes in pore geometry. Although
 492 direct monitoring of these effects was not possible, their influence is expected to be limited in
 493 a homogeneous sand pack, yet they should still be considered when interpreting the results.
 494 Additionally, acoustic response may depend on the freezing and melting history (Dou et al.,
 495 2016; Li and Matsushima, 2024). Ice distribution during melting may not perfectly match that
 496 during freezing, especially if drainage pathways, air entrapment, or dilation effects differ. Such
 497 hysteresis could influence acoustic properties and should be tested in future experiments.

498 Finally, fresh and saline water may coexist in natural permafrost. Although salinity has
499 minimal effect on compressional velocity and no measurable effect on attenuation (Jones et al.,
500 1998; Toksöz et al., 1979), it lowers the freezing point and thereby influences ice formation
501 within the porous medium. This effect becomes particularly significant near full ice saturation,
502 where salinity can lead to a more gradual velocity change (Lyu et al., 2020). These limitations
503 open future research directions towards enhancing real-time monitoring of permafrost
504 environments, which include repeating tests on different sediment types, measuring
505 complementary parameters for a more thorough understanding of the freezing point, and
506 upscaling laboratory results into real case in-field scenarios.

507

508

9CONCLUSION

509

510

511

512

An acoustic pulse tube was used to investigate the effect of ice content on velocity and
attenuation in ice-bearing sands during melting, across a frequency range of 1–20 kHz, at three
effective pressures (2.5, 5.0 & 7.5 MPa). The results serve as an analog for permafrost
conditions at depths between approximately 150 and 450 m.

513

514

515

516

517

518

519

Ice content significantly affects the acoustic properties of the sediment. Velocity
decrease occurs at all pressures, with the largest change observed at the lowest effective
pressure (2.5 MPa), where weaker grain-to-grain contact allows ice to exert greater influence
on the acoustic response. Additionally, attenuation increases as the ice melts, peaking at lower
saturation under lower pressures and at higher saturations under higher pressures. This
extension of findings further highlights the relationship between effective pressure and the
acoustic behavior of ice-bearing sediments.

520

521

522

523

524

Both velocity and attenuation exhibit non-linear behavior with changes in ice content.
Their correlation suggests that combining both parameters could potentially be used to infer ice
content at given depths within the effective pressure range of 2.5 - 7.5 MPa. Comparison with
Biot three-phase models indicates that ice distribution significantly affects velocity, while
attenuation is more influenced by pore structure, reflecting ice morphologies (the proportion of

525 pore-filling to cementing ice) and the sediment frame's permeability, as well as pressure
526 conditions.

527 Compared to studies at ultrasonic frequencies, the lower-frequency measurements used
528 in this study provide insights at scales relevant to field applications. These findings highlight
529 the importance of understanding ice saturation, distribution, and morphology for accurately
530 predicting acoustic wave behavior in ice-bearing sediments, with potential applications for
531 permafrost monitoring.

532

533 **DATA AND MATERIALS AVAILABILITY**

534 Data associated with this research are available and can be accessed via the following
535 URL: <https://doi.org/10.5258/SOTON/D3398>.

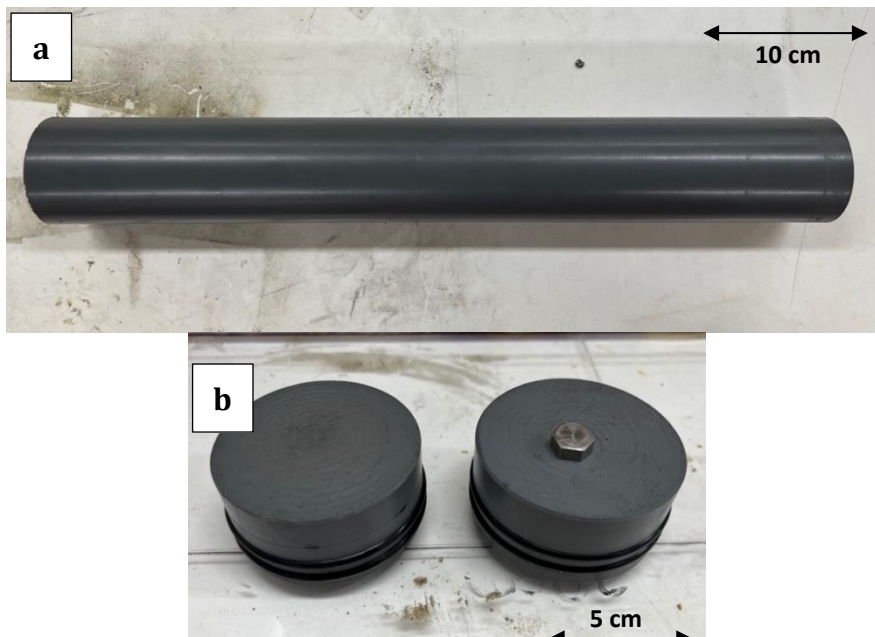
536

APPENDICES

537 **Appendix A. Sample preparation**

538 The samples were prepared by pouring sand into the PVC pipe and compacting it layer
539 by layer. Both ends of the pipe were sealed with PVC caps (Figure A.1), which had rubber O-
540 rings that maintained a seal while allowing the surrounding fluid (water) to apply even
541 hydrostatic pressure on the sand. The top of each layer was lightly scratched to avoid impedance
542 differences between layers. The process was repeated until the pipe was fully compacted,
543 leaving room for the top cap. We saturated the sand by gradually introducing de-ionized water,
544 increasing saturation in steps by around 10%. To remove air bubbles during saturation, the pipe
545 was tapped continuously. Once saturation was achieved, the top cap was sealed, and the sample
546 was left for 24 hours before the water-saturated pulse tube measurement. Uncertainty of the
547 sample's porosity was calculated using error propagation methods. We measured empirical
548 porosity (ϕ) using the wet-dry mass method and compared it with theoretical porosity (ϕ_T) based
549 on bulk dry (ρ_b) and grain (ρ_s) densities, using the formula $\phi_T = 1 - \rho_b / \rho_s$. This approach helped
550 the assessment of uncertainties related to the saturation process due to non-connected porosity,
551 leading to ice saturation errors of $\sim 7\%$.

552



553

554 *Figure A.1 PVC jacket system used to enable sample emplacement inside the water-filled*
555 *acoustic pulse tube: a) 50 cm length PVC cylinder jacket, and b) top and bottom PVC endcaps*
556 *with O-ring seals, including the location of the pore fluid vent port (shown as a hexagonal nut*
557 *on the top endcap on the right).*

558 Appendix B. Inferring ice saturation and additional rock physic modeling results

559 We first established a baseline by measuring the velocity and attenuation of the sample
560 in its fully melted state ($S_i = 0$) to serve as a comparison for the measurements taken during the
561 melting process. At the start, we assumed an initial ice saturation ($S_i = 1$) when the sample was
562 placed in the pulse tube, though some unfrozen water likely remained, such as thin water films
563 bound to the grains (Watanabe and Mizoguchi, 2002). However, due to the time needed to reach
564 the target pressure in the pulse tube, measurements at full ice saturation ($S_i = 1$) were not
565 possible, as some melting had already occurred. Instead, we used a regression model to estimate
566 velocity and attenuation at full saturation.

567 We estimated ice saturation based on the melting time during the measurements,
568 applying an empirical relationship (Equation B.1):

$$S_i = 1 - \left(\frac{t}{T}\right)^n, \quad (\text{B.1})$$

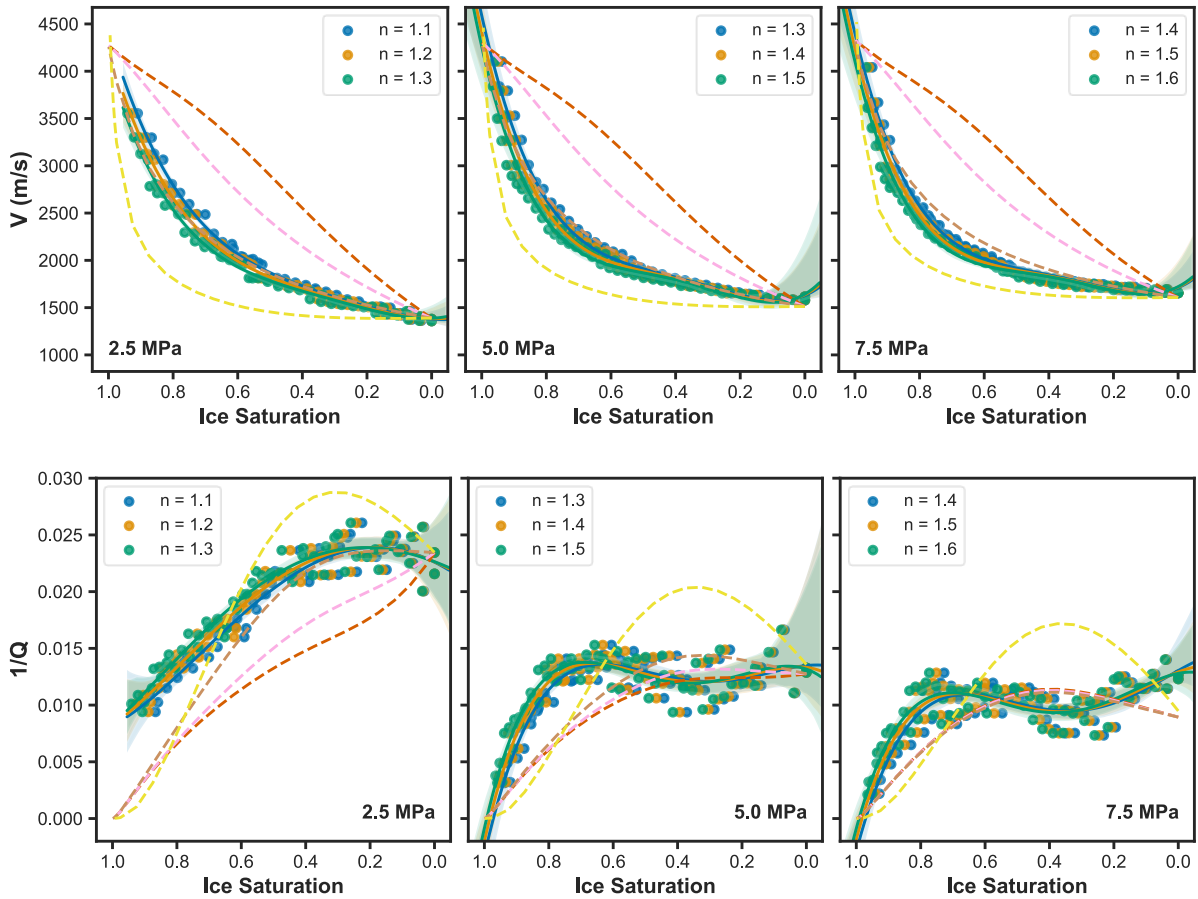
569 where S_i represents ice saturation, t is the time elapsed during measurement (in seconds),
570 T is the total time for complete melting (determined by the velocity and attenuation at the fully
571 melted state), and n is an empirical parameter describing the exponential relationship between
572 ice melting and time. We derived the value of n by comparing experimental results with three-
573 phase rock physics models (Leclaire et al., 1994; Marín-Moreno et al., 2017) using visual
574 comparison and by minimizing the objective function (Equation B.2). The function performs
575 well when velocity and attenuation show similar variations, as in the current dataset. However,
576 if their variation magnitudes differ significantly, one parameter may dominate the objective
577 function. Thus, the method is most effective when both parameters vary comparably.

Objective function

$$= \frac{|V_{\text{experimental}} - V_{\text{modelled}}|}{V_{\text{experimental}}} + \frac{|Q_{\text{experimental}}^{-1} - Q_{\text{modelled}}^{-1}|}{Q_{\text{experimental}}^{-1}} \quad (\text{B.2})$$

578 Figure B.1 illustrates the closest fit between the measured and calculated velocity and
579 attenuation, while Table B.1 provides the objective function outcomes. To determine the
580 empirical parameter n , we considered two factors: the best fit between experimental data and

581 model predictions using the objective function (Equation B.2), and how well the predicted
 582 experimental values at $S_i = 1$ (from regression models) matched the model results. We found
 583 that experimental velocity matched the models best when n was 1.2, 1.3, and 1.5 for the 2.5, 5,
 584 and 7.5 MPa datasets, respectively. While velocity comparisons are straightforward, the
 585 attenuation data required the objective function to better determine the n value.
 586

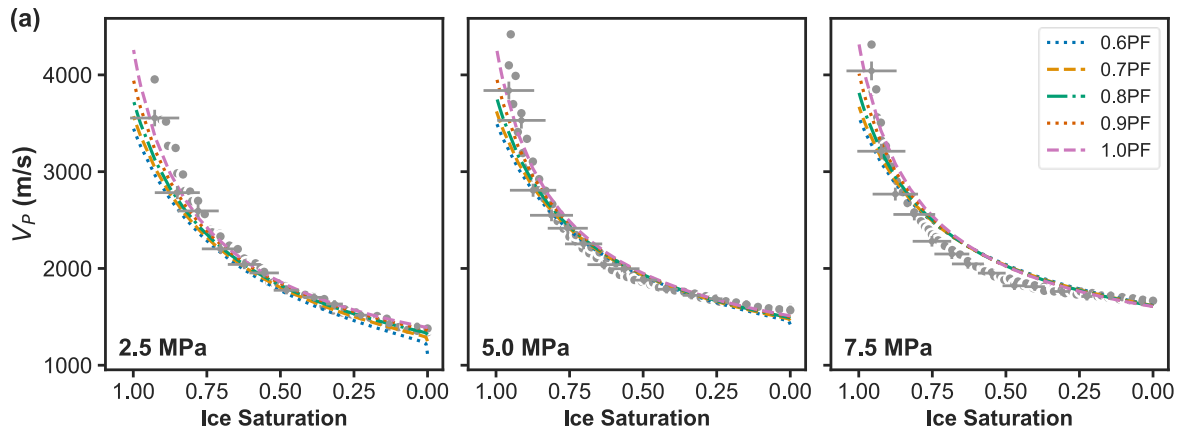


587

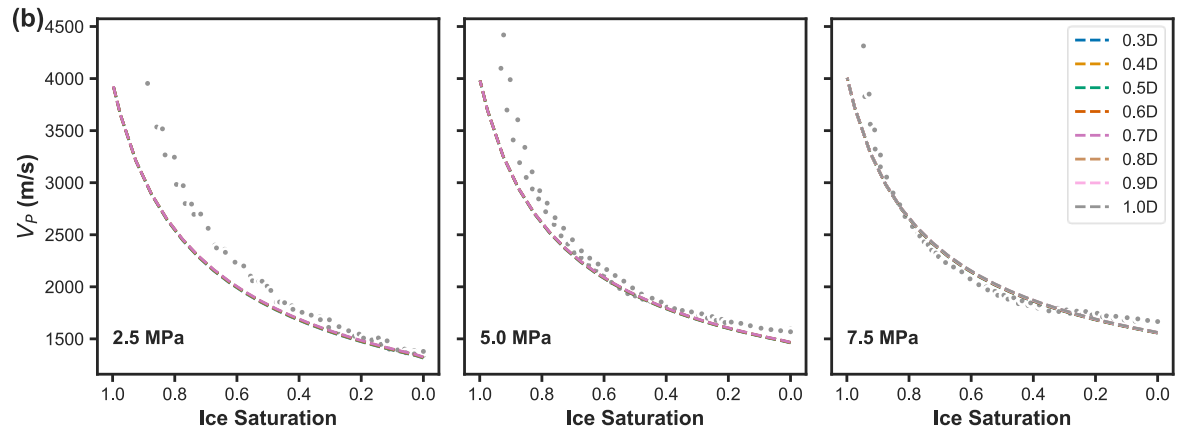
588

589 **Figure B.1** Empirical parameter (n) fitting of measured data at 10 kHz (indicated by the legend)
 590 of velocity (top) and attenuation (bottom) to HBES with Reuss, Brie, and Voigt approximations
 591 (red, pink, and brown dashed lines, respectively) and LeClaire (yellow dashed lines) models.
 592 Blue, orange, and green lines represent the respective regression models for each dataset, with
 593 an averaged R^2 of 0.98 and 0.85 for velocity and attenuation, respectively.

594



595



596

597 **Figure B.2** Comparison of experimental (data points) and modeled velocities (dashed lines):
 598 a) at various pore-filling (PF) saturation of ice, and b) at various permeabilities (in Darcies
 599 $[D] = 1 \times 10^{-12} \text{ m}^2$) for PF = 1.0, using the HBES model with Voigt approximations.

600

601 **Table B.1** Calculation of objective functions to compare experimental and modelled velocity
 602 and attenuation. Best fits are indicated by lowest values (underlined).

Dataset	Objective function at $n =$				
	1.1	1.2	1.3	1.4	1.5
2.5 MPa	0.359	0.349	0.351	0.359	0.375
5 MPa	0.317	0.416	0.314	0.403	0.333
7.5 MPa	0.721	0.655	0.596	0.531	0.467

603

REFERENCES

- Abbasi, M., Mousavi, S.M., Lee, B.J., Esfahani, J.A., Karimi, N., Mamaghani, M.Y., 2022. Examination of the effects of porosity upon intensification of thermal storage of PCMs in a shell-and-tube type system. *Case Stud. Therm. Eng.* 33, 101963. <https://doi.org/10.1016/j.csite.2022.101963>
- Alkire, B.D., Andersland, O.B., 1973. The Effect of Confining Pressure on the Mechanical Properties of Sand–Ice Materials. *J. Glaciol.* 12, 469–481. <https://doi.org/10.3189/S0022143000031889>
- Allmark, C., Curtis, A., Galetti, E., De Ridder, S., 2018. Seismic Attenuation From Ambient Noise Across the North Sea Ekofisk Permanent Array. *J. Geophys. Res. Solid Earth* 123, 8691–8710. <https://doi.org/10.1029/2017JB015419>
- Berryman, J.G., 1981. Elastic wave propagation in fluid-saturated porous media II. *J. Acoust. Soc. Am.* 70, 1754–1756. <https://doi.org/10.1121/1.387193>
- Best, A.I., Priest, J.A., Clayton, C.R.I., Rees, E.V.L., 2013. The effect of methane hydrate morphology and water saturation on seismic wave attenuation in sand under shallow sub-seafloor conditions. *Earth Planet. Sci. Lett.* 368, 78–87. <https://doi.org/10.1016/j.epsl.2013.02.033>
- Biot, M.A., 1956a. Theory of Propagation of Elastic Waves in a Fluid-Saturated Porous Solid. I. Low-Frequency Range. *J. Acoust. Soc. Am.* 28, 168–178. <https://doi.org/10.1121/1.1908239>
- Biot, M.A., 1956b. Theory of Propagation of Elastic Waves in a Fluid-Saturated Porous Solid. II. Higher Frequency Range. *J. Acoust. Soc. Am.* 28, 179–191. <https://doi.org/10.1121/1.1908241>
- Brie, A., Pampuri, F., Marsala, A.F., Meazza, O., 1995. Shear Sonic Interpretation in Gas-Bearing Sands. Presented at the SPE Annual Technical Conference and Exhibition, p. SPE-30595-MS. <https://doi.org/10.2118/30595-MS>
- Bustamante, J., Fabien-Ouellet, G., Duchesne, M.J., Ibrahim, A., 2023. Understanding seismic velocity variations of subsea permafrost: A sensitivity study. *Geophysics* R655–R669. <https://doi.org/10.1190/geo2022-0568.1>
- Carcione, J.M., Helle, H.B., Pham, N.H., 2003. White's model for wave propagation in partially saturated rocks: Comparison with poroelastic numerical experiments. *GEOPHYSICS* 68, 1389–1398. <https://doi.org/10.1190/1.1598132>
- Chang, X., Liu, W., Zuo, G., Dou, Y., Li, Y., 2021. Research on ultrasonic-based investigation of mechanical properties of ice. *Acta Oceanol. Sin.* 40, 97–105. <https://doi.org/10.1007/s13131-021-1890-3>
- Dash, J.G., Fu, H., Wettlaufer, J.S., 1995. The premelting of ice and its environmental consequences. *Rep. Prog. Phys.* 58, 115–167. <https://doi.org/10.1088/0034-4885/58/1/003>
- De Lemos, M.J.S., 2012. Applications in Hybrid Media, in: *Turbulence in Porous Media*. Elsevier, pp. 199–352. <https://doi.org/10.1016/B978-0-08-098241-0.00011-5>
- Desai, K.P., Moore, E.J., 1968. Well Log Interpretation In Permafrost. *Log Anal.* 9.
- Dobiński, W., 2020. Permafrost active layer. *Earth-Sci. Rev.* 208, 103301. <https://doi.org/10.1016/j.earscirev.2020.103301>
- Dou, S., Nakagawa, S., Dreger, D., Ajo-Franklin, J., 2016. A rock-physics investigation of unconsolidated saline permafrost: P-wave properties from laboratory ultrasonic

- measurements. *Geophysics* 81, WA233–WA245. <https://doi.org/10.1190/geo2015-0176.1>
- Dvorkin, J., Prasad, M., Sakai, A., Lavoie, D., 1999. Elasticity of marine sediments: Rock physics modeling. *Geophys. Res. Lett.* 26, 1781–1784. <https://doi.org/10.1029/1999GL900332>
- Ecker, C., Dvorkin, J., Nur, A., 1998. Sediments with gas hydrates: Internal structure from seismic AVO. *Geophysics* 63, 1659–1669.
- Ecker, C., Dvorkin, J., Nur, A.M., 2000. Estimating the amount of gas hydrate and free gas from marine seismic data. *Geophysics* 65, 565–573. <https://doi.org/10.1190/1.1444752>
- Emerson, M., Foray, P., 2006. Laboratory P-wave measurements in dry and saturated sand. *Acta Geotech.* 1, 167–177. <https://doi.org/10.1007/s11440-006-0015-7>
- Falcon-Suarez, I.H., Amalokwu, K., Delgado-Martin, J., Callow, B., Robert, K., North, L., Sahoo, S.K., Best, A.I., 2019. Comparison of stress-dependent geophysical, hydraulic and mechanical properties of synthetic and natural sandstones for reservoir characterization and monitoring studies. *Geophys. Prospect.* 67, 784–803. <https://doi.org/10.1111/1365-2478.12699>
- French, H.M., 2007. Permafrost, in: *The Periglacial Environment*. pp. 83–115. <https://doi.org/10.1002/9781118684931.ch5>
- Fuchs, M., Grosse, G., Jones, B.M., Strauss, J., Baughman, C.A., Walker, D.A., 2018. Sedimentary and geochemical characteristics of two small permafrost-dominated Arctic river deltas in northern Alaska. *arktos* 4, 1–18. <https://doi.org/10.1007/s41063-018-0056-9>
- Hearst, J.R., Nelson, P.H., 1985. *Well logging for physical properties*. Mc Graw-Hill Book Co, United States.
- Hefner, B.T., Jackson, D.R., Calantoni, J., Reed, A.H., 2006. Dispersion and attenuation due to scattering from heterogeneities in the porosity of sand sediments. *J. Acoust. Soc. Am.* 120, 3098–3099. <https://doi.org/10.1121/1.4787533>
- Helgerud, M.B., Dvorkin, J., Nur, A., Sakai, A., Collett, T., 1999. Elastic-wave velocity in marine sediments with gas hydrates: Effective medium modeling. *Geophys. Res. Lett.* 26, 2021–2024. <https://doi.org/10.1029/1999GL900421>
- Helgerud, M.B., Waite, W.F., Kirby, S.H., Nur, A., 2009. Elastic wave speeds and moduli in polycrystalline ice Ih, sI methane hydrate, and sII methane-ethane hydrate. *J. Geophys. Res.* 114, B02212. <https://doi.org/10.1029/2008JB006132>
- Hilbich, C., Hauck, C., Mollaret, C., Wainstein, P., Arenson, L.U., 2022. Towards accurate quantification of ice content in permafrost of the Central Andes – Part 1: Geophysics-based estimates from three different regions. *The Cryosphere* 16, 1845–1872. <https://doi.org/10.5194/tc-16-1845-2022>
- Hjort, J., Karjalainen, O., Aalto, J., Westermann, S., Romanovsky, V.E., Nelson, F.E., Etzelmüller, B., Luoto, M., 2018. Degrading permafrost puts Arctic infrastructure at risk by mid-century. *Nat. Commun.* 9, 5147. <https://doi.org/10.1038/s41467-018-07557-4>
- Hu, G., Ye, Y., Liu, C., Best, A., Li, C., 2014. Gas hydrate distribution in sediment pore space and its impact on acoustic properties of hydrate-bearing sediments, in: *Proceedings of the 8th International Conference on Gas Hydrates*.

- Jones, S.M., McCann, C., Astin, T.R., Sothcott, J., 1998. The effects of pore-fluid salinity on ultrasonic wave propagation in sandstones. *GEOPHYSICS* 63, 928–934. <https://doi.org/10.1190/1.1444404>
- Kang, S., Jin, Y.K., Jang, U., Duchesne, M.J., Shin, C., Kim, S., Riedel, M., Dallimore, S.R., Paull, C.K., Choi, Y., Hong, J.K., 2021. Imaging the P-Wave Velocity Structure of Arctic Subsea Permafrost Using Laplace-Domain Full-Waveform Inversion. *J. Geophys. Res. Earth Surf.* 126, e2020JF005941. <https://doi.org/10.1029/2020JF005941>
- Kawasaki, K., Osterkamp, T.E., Jurick, R.W., Kienle, J., 1983. Gravity Measurements in Permafrost Terrain Containing Massive Ground Ice. *Ann. Glaciol.* 4, 133–140. <https://doi.org/10.3189/S026030550000536X>
- Kim, I.-W., Timmermann, A., Kim, J.-E., Rodgers, K.B., Lee, S.-S., Lee, H., Wieder, W.R., 2024. Abrupt increase in Arctic-Subarctic wildfires caused by future permafrost thaw. *Nat. Commun.* 15, 7868. <https://doi.org/10.1038/s41467-024-51471-x>
- Kolsky, H., 1964. Stress waves in solids. *J. Sound Vib.* 1, 88–110. [https://doi.org/https://doi.org/10.1016/0022-460X\(64\)90008-2](https://doi.org/https://doi.org/10.1016/0022-460X(64)90008-2)
- Leclaire, Ph., Cohen-Ténoudji, F., Aguirre-Puente, J., 1994. Extension of Biot's theory of wave propagation to frozen porous media. *J. Acoust. Soc. Am.* 96, 3753–3768. <https://doi.org/10.1121/1.411336>
- Lee, J.-W., Kim, J.-S., Hong, C.-H., Oh, T.-M., 2024. Permeability monitoring of underground concrete structures using elastic wave characteristics with modified Biot's model. *Sci. Rep.* 14, 22110. <https://doi.org/10.1038/s41598-024-73449-x>
- Li, B., Matsushima, J., 2024. Influence of ice properties on wave propagation characteristics in partially frozen soils and rocks: A temperature-dependent rock-physics model. *Geophysics* 89, MR281–MR295. <https://doi.org/10.1190/geo2023-0694.1>
- Lin, Z., Pan, H., Fang, H., Gao, W., Liu, D., 2018. High-altitude well log evaluation of a permafrost gas hydrate reservoir in the Muli area of Qinghai, China. *Sci. Rep.* 8, 12596. <https://doi.org/10.1038/s41598-018-30795-x>
- Liu, L., Zang, S., Wu, X., Liu, R., Li, T., Zhu, J., Sun, L., Wu, S., Dong, X., Zhang, Z., 2023. Sediment Grain-Size Composition in the Permafrost Region of the Greater Khingan Range and Its Significance as a Material Source. *Land* 12, 1728. <https://doi.org/10.3390/land12091728>
- Lyu, C., Amiri, S.A.G., Grimstad, G., Høyland, K.V., Ingeman-Nielsen, T., 2020. Comparison of Geoacoustic Models for Unfrozen Water Content Estimation. *J. Geophys. Res. Solid Earth* 125, e2020JB019766. <https://doi.org/10.1029/2020JB019766>
- Mahabadi, N., Dai, S., Seol, Y., Jang, J., 2019. Impact of hydrate saturation on water permeability in hydrate-bearing sediments. *J. Pet. Sci. Eng.* 174, 696–703. <https://doi.org/10.1016/j.petrol.2018.11.084>
- Marín-Moreno, H., Sahoo, S.K., Best, A.I., 2017. Theoretical modeling insights into elastic wave attenuation mechanisms in marine sediments with pore-filling methane hydrate: Hydrate-Bearing Effective Sediment Model. *J. Geophys. Res. Solid Earth.* <https://doi.org/10.1002/2016JB013577>
- Matsushima, J., Suzuki, M., Kato, Y., Rokugawa, S., 2016. Ultrasonic measurements of attenuation and velocity of compressional and shear waves in partially frozen unconsolidated sediment and synthetic porous rock. *Geophysics* 81, D141–D153. <https://doi.org/10.1190/geo2015-0350.1>

- Mavko, G., Mukerji, T., Dvorkin, J., 2009. *The Rock Physics Handbook*, 2nd ed. Cambridge University Press.
- McCann, C., Sothcott, J., Best, A.I., 2014. A new laboratory technique for determining the compressional wave properties of marine sediments at sonic frequencies and *in situ* pressures: Compressional wave properties of marine sediments. *Geophys. Prospect.* 62, 97–116. <https://doi.org/10.1111/1365-2478.12079>
- McCutchan, A., Johnson, B., 2022. Laboratory Experiments on Ice Melting: A Need for Understanding Dynamics at the Ice-Water Interface. *J. Mar. Sci. Eng.* 10, 1008. <https://doi.org/10.3390/jmse10081008>
- Meredith, M., Sommerkorn, M., Casotta, S., Derksen, C., Ekaykin, A., Hollowed, A., Kofinas, G., Mackintosh, A., Melbourne-Thomas, J., Muelbert, M., Ottersen, G., Pritchard, H., Schuur, E., 2022. *The Ocean and Cryosphere in a Changing Climate: Special Report of the Intergovernmental Panel on Climate Change*, 1st ed. Cambridge University Press. <https://doi.org/10.1017/9781009157964>
- Mindlin, R.D., 1949. Compliance of Elastic Bodies in Contact. *J. Appl. Mech.* 16, 259–268. <https://doi.org/10.1115/1.4009973>
- Mobley, J., Waters, K.R., Hughes, M.S., Hall, C.S., Marsh, J.N., Brandenburger, G.H., Miller, J.G., 2000. Kramers–Kronig relations applied to finite bandwidth data from suspensions of encapsulated microbubbles. *J. Acoust. Soc. Am.* 108, 2091–2106. <https://doi.org/10.1121/1.1312364>
- Müller, T.M., Gurevich, B., Lebedev, M., 2010. Seismic wave attenuation and dispersion resulting from wave-induced flow in porous rocks — A review. *Geophysics* 75. <https://doi.org/10.1190/1.3463417>
- Murphy, W.F., 1982. *Effects of Microstructure and Pore Fluids on the Acoustic Properties of Granular Sedimentary Materials*, Stanford Rock Physics Project report. Stanford University.
- Nakano, Y., Arnold, R., 1973. Acoustic properties of frozen Ottawa sand. *Water Resour. Res.* 9, 178–184. <https://doi.org/10.1029/WR009i001p00178>
- North, L., Best, A., 2015. An Improved High-Spectral Resolution Water Filled Impedance Tube Measurement Method For Marine Sediment Studies, in: *Seabed and Sediment Acoustics 2015*. Presented at the Seabed and Sediment Acoustics 2015, Institute of Acoustics, Bath. <https://doi.org/10.25144/18070>
- Osterkamp, T.E., Payne, M.W., 1981. Estimates of permafrost thickness from well logs in northern Alaska. *Cold Reg. Sci. Technol.* 5, 13–27. [https://doi.org/10.1016/0165-232X\(81\)90037-9](https://doi.org/10.1016/0165-232X(81)90037-9)
- Oswell, J.M., 2011. Pipelines in permafrost: geotechnical issues and lessons ¹ 2010 R.M. Hardy Address, 63rd Canadian Geotechnical Conference. *Can. Geotech. J.* 48, 1412–1431. <https://doi.org/10.1139/t11-045>
- Parolai, S., Lai, C.G., Dreossi, I., Ktenidou, O.-J., Yong, A., 2022. A review of near-surface QS estimation methods using active and passive sources. *J. Seismol.* 26, 823–862. <https://doi.org/10.1007/s10950-021-10066-5>
- Priest, J.A., Abbas, M., Hayley, J.L., 2021. The Change in Geomechanical Properties of Gas Saturated Methane Hydrate-Bearing Sand Resulting From Water Saturation. *J. Geophys. Res. Solid Earth* 126. <https://doi.org/10.1029/2021JB022245>

- Priest, J.A., Rees, E.V.L., Clayton, C.R.I., 2009. Influence of gas hydrate morphology on the seismic velocities of sands. *J. Geophys. Res. Solid Earth* 114, 2009JB006284. <https://doi.org/10.1029/2009JB006284>
- Redwood, Martin., 1960. *Mechanical waveguides; the propagation of acoustic and ultrasonic waves in fluids and solids with boundaries*. Pergamon Press, New York.
- Reuss, A., 1929. Berechnung der Fließgrenze von Mischkristallen auf Grund der Plastizitätsbedingung für Einkristalle. *Z. Für Angew. Math. Mech.* 9, 49–58. <https://doi.org/10.1002/zamm.19290090104>
- Rubino, J.G., Holliger, K., 2012. Seismic attenuation and velocity dispersion in heterogeneous partially saturated porous rocks: Mesoscopic effects and partial saturation. *Geophys. J. Int.* 188, 1088–1102. <https://doi.org/10.1111/j.1365-246X.2011.05291.x>
- Sahoo, S.K., Best, A.I., 2021. The Influence of Gas Hydrate Morphology on Reservoir Permeability and Geophysical Shear Wave Remote Sensing. *J. Geophys. Res. Solid Earth* 126. <https://doi.org/10.1029/2021JB022206>
- Sahoo, S.K., Madhusudhan, B.N., Marín-Moreno, H., North, L.J., Ahmed, S., Falcon-Suarez, I.H., Minshull, T.A., Best, A.I., 2018. Laboratory Insights Into the Effect of Sediment-Hosted Methane Hydrate Morphology on Elastic Wave Velocity From Time-Lapse 4-D Synchrotron X-Ray Computed Tomography. *Geochem. Geophys. Geosystems* 19, 4502–4521. <https://doi.org/10.1029/2018GC007710>
- Schumann, K., Stipp, M., Behrmann, J.H., Klaeschen, D., Schulte-Kortnack, D., 2014. *P* and *S* wave velocity measurements of water-rich sediments from the Nankai Trough, Japan: *P*- and *S*-wave velocity measurements. *J. Geophys. Res. Solid Earth* 119, 787–805. <https://doi.org/10.1002/2013JB010290>
- Schuur, E.A.G., McGuire, A.D., Schädel, C., Grosse, G., Harden, J.W., Hayes, D.J., Hugelius, G., Koven, C.D., Kuhry, P., Lawrence, D.M., Natali, S.M., Olefeldt, D., Romanovsky, V.E., Schaefer, K., Turetsky, M.R., Treat, C.C., Vonk, J.E., 2015. Climate change and the permafrost carbon feedback. *Nature* 520, 171–179. <https://doi.org/10.1038/nature14338>
- Selfridge, A.R., 1985. Approximate Material Properties in Isotropic Materials. *IEEE Trans. Sonics Ultrason.* 32, 381–394. <https://doi.org/10.1109/T-SU.1985.31608>
- Simmons, G., 1965. Single Crystal Elastic Constants and Calculated Aggregate Properties 274.
- Sizemore, H.G., Mellon, M.T., 2008. Laboratory characterization of the structural properties controlling dynamical gas transport in Mars-analog soils. *Icarus* 197, 606–620. <https://doi.org/10.1016/j.icarus.2008.05.013>
- Snehota, M., Jelinkova, V., Sobotkova, M., Sacha, J., Vontobel, P., Hovind, J., 2015. Water and entrapped air redistribution in heterogeneous sand sample: Quantitative neutron imaging of the process. *Water Resour. Res.* 51, 1359–1371. <https://doi.org/10.1002/2014WR015432>
- Spangenberg, E., Seyberth, K., Heeschen, K.U., Priegnitz, M., Schicks, J.M., 2018. A *Quick Look* Method to Assess the Dependencies of Rock Physical Sediment Properties on the Saturation With Pore-Filling Hydrate. *J. Geophys. Res. Solid Earth* 123, 5588–5598. <https://doi.org/10.1029/2018JB015855>
- Strauss, J., Schirrmeister, L., Wetterich, S., Borchers, A., Davydov, S.P., 2012. Grain-size properties and organic-carbon stock of Yedoma Ice Complex permafrost from the

- Kolyma lowland, northeastern Siberia. *Glob. Biogeochem. Cycles* 26, 2011GB004104. <https://doi.org/10.1029/2011GB004104>
- Sutiyoso, H.S., 2025. A Laboratory Acoustic Study of Fluid and Ice Saturation Effects in Sands. University of Southampton, Southampton.
- Sutiyoso, H.S., Sahoo, S.K., North, L.J., Falcon-Suarez, I.H., Minshull, T.A., Best, A.I., 2025. Laboratory Measurement of Sonic (1–20 kHz) P-Wave Velocity and Attenuation During Melting of Ice-Bearing Sand. *J. Geophys. Res. Solid Earth* 130, e2024JB030465. <https://doi.org/10.1029/2024JB030465>
- Sutiyoso, H.S., Sahoo, S.K., North, L.J., Minshull, T.A., Falcon-Suarez, I.H., Best, A.I., 2024. Laboratory measurements of water saturation effects on the acoustic velocity and attenuation of sand packs in the 1–20 kHz frequency range. *Geophys. Prospect.* <https://doi.org/10.1111/1365-2478.13607>
- Toksöz, M.N., Johnston, D.H., Timur, A., 1979. Attenuation of seismic waves in dry and saturated rocks: I. Laboratory measurements. *Geophysics* 44, 681–690. <https://doi.org/10.1190/1.1440969>
- Voigt, W., 1889. Ueber die Beziehung zwischen den beiden Elasticitätsconstanten isotroper Körper. *Ann. Phys.* 274, 573–587. <https://doi.org/10.1002/andp.18892741206>
- Wagner, W., Riethmann, T., Feistel, R., Harvey, A.H., 2011. New Equations for the Sublimation Pressure and Melting Pressure of H₂O Ice Ih. *J. Phys. Chem. Ref. Data* 40, 043103. <https://doi.org/10.1063/1.3657937>
- Watanabe, K., Mizoguchi, M., 2002. Amount of unfrozen water in frozen porous media saturated with solution. *Cold Reg. Sci. Technol.* 34, 103–110. [https://doi.org/10.1016/S0165-232X\(01\)00063-5](https://doi.org/10.1016/S0165-232X(01)00063-5)
- Wu, R., Aki, K., 1985. Scattering characteristics of elastic waves by an elastic heterogeneity. *GEOPHYSICS* 50, 582–595. <https://doi.org/10.1190/1.1441934>
- Yang, L., Jia, H., Han, L., Zhang, H., Tang, L., 2021. Hysteresis in the ultrasonic parameters of saturated sandstone during freezing and thawing and correlations with unfrozen water content. *J. Rock Mech. Geotech. Eng.* 13, 1078–1092. <https://doi.org/10.1016/j.jrmge.2021.06.006>
- Zimmer, M., 2003. Seismic velocities in unconsolidated sands: measurements of pressure, sorting and compaction effects.
- Zimmer, M., Prasad, M., Mavko, G., 2002. Pressure and porosity influences on VP–VS ratio in unconsolidated sands. *Lead. Edge* 21, 178–183. <https://doi.org/10.1190/1.1452609>

LIST OF FIGURES

- Figure 1** Comparison of compressional velocity (V_P) of water-saturated sand measured in this study with values reported in published studies. The three data points for this study represent measurements at different effective pressures (2.5, 5.0, and 7.5 MPa), with error bars indicating experimental uncertainty. Marker size represents the confining pressure, ranging from atmospheric pressure to 10 MPa. The study codes are as follows: KG (Kang et al., 2021), YG (Yang et al., 2021), SP (Spangenberg et al., 2018), DOU (Dou et al., 2016), and NAKA (Nakano and Arnold, 1973). 7
- Figure 2** Experimental apparatus and resulting raw and processed data: (a) Schematic diagram of the pulse tube with dimensions; (b) details of the PVC-jacketed sample inside the water-filled pulse tube; (c) raw time-series signals acquired during measurements; (d) deconvolved signals for water-saturated and ice-bearing sand samples on both hydrophones (see panel (a) for hydrophone positions)..... 8
- Figure 3** Variations in P-wave velocity (V_P) and attenuation ($1/Q_P$) at 10 kHz during the ice melting process at various effective pressures, with shaded areas representing fourth-order polynomial regression models with a confidence interval of 90% (R^2 of 0.99, 0.98, 0.98 for velocity and 0.94, 0.82, 0.79 for attenuation at 2.5, 5, and 7.5 MPa, respectively). Error bars are plotted every 10 data points. 12
- Figure 4** Experimental results: a) P-wave velocity (V_P) and b) attenuation ($1/Q_P$) spectra at selected ice saturations (S_i). The error bars are smaller than the symbol sizes. Legends represent effective pressures in megapascals (MPa). 13
- Figure 5** Regression slope of P-wave velocity (V_P) versus frequency between the cut-off and maximum (20 kHz) frequencies as a function of ice saturations and effective pressures. Positive slopes indicate velocity increasing with frequency, while negative slopes indicate velocity decreasing with frequency. Legends represent effective pressures in megapascals (MPa)..... 14
- Figure 6** Spearman's rank correlation coefficients between acoustic properties (P-wave velocity, V_P and attenuation, $1/Q_P$) and ice saturation, calculated at each frequency and effective pressure (in megapascals). The vertical axis ranges from -1 to +1 to accommodate both positive (typically for velocity) and negative (typically for attenuation) correlations. The 90% and 99% confidence level lines apply to both acoustic properties and indicate statistically significant correlations.... 15
- Figure 7** Comparison of experimental data and model results for P-waves at 10 kHz: a) velocity (V_P) and b) attenuation ($1/Q_P$). In the HBES models, the pore-filling saturation PF is 1.0 and the permeability is 0.5 D; c) attenuation at different PF (with the remainder of S_i as cementing ice, i.e., $1 - PF$); and d) attenuation at different permeabilities for $PF = 1.0$. Results in c) and d) are modeled using the HBES model with Voigt approximation. Cross-error bars are plotted every 15 experimental data points. 18

Figure 8 Variations in P-wave velocity (V_P) and attenuation ($1/Q_P$) at 10 kHz plotted against each other, with lines representing second-order polynomial regression models with R^2 of 0.94, 0.72, and 0.72 at 2.5, 5, and 7.5 MPa, respectively. Marker types represent different effective pressures as shown in the legend. Cross-error bars are plotted every 15 data points. 22

Figure A.1 PVC jacket system used to enable sample emplacement inside the water-filled acoustic pulse tube: a) 50 cm length PVC cylinder jacket, and b) top and bottom PVC endcaps with O-ring seals, including the location of the pore fluid vent port (shown as a hexagonal nut on the top endcap on the right). **Error! Bookmark not defined.**

Figure B.1 Empirical parameter (n) fitting of measured data at 10 kHz (indicated by the legend) of velocity (top) and attenuation (bottom) to HBES with Reuss, Brie, and Voigt approximations (red, pink, and brown dashed lines, respectively) and LeClaire (yellow dashed lines) models. Blue, orange, and green lines represent the respective regression models for each dataset with an averaged R^2 of 0.98 and 0.85 for velocity and attenuation, respectively. 27

Figure B.2 Comparison of experimental and modelled velocities: a) at various pore-filling (PF) saturation of ice, and b) at various permeabilities (in Darcies $[D] = 1 \times 10^{-12} \text{ m}^2$) for PF = 1.0, using the HBES model with Voigt approximations. 28

LIST OF TABLES

Table 1 Fixed and case-dependent input parameters used in the model runs (case-dependent parameters are used only in HBES model runs). 10

Table B.1 Calculation of objective functions to compare experimental and modelled velocity and attenuation. Best fits are indicated by lowest values (underlined). 28